NASA Technical Memorandum 104329

Inlet Distortion for an F/A-18A Aircraft During Steady Aerodynamic Conditions up to 60° Angle of Attack

Kevin R. Walsh, Andrew J. Yuhas, John G. Williams and William G. Steenken

NASA Contract NAS 3-26617
April 1997

National Aeronautics and
Space Administration

NASA Technical Memorandum 104329

Inlet Distortion for an F/A-18A Aircraft During Steady Aerodynamic Conditions up to 60° Angle of Attack

Kevin R. Walsh
NASA Dryden Flight Research Center
Edwards, California

Andrew J. Yuhas
Analytical Services and Materials
Hampton, Virginia

John G. Williams and William G. Steenken
General Electric Aircraft Engines
Evendale, Ohio

Under NASA Dryden Flight Research Center
Contract NAS 3-26617

1997

National Aeronautics and
Space Administration

Dryden Flight Research Center
Edwards, California 93523-0273

NOTICE

Use of trade names or names of manufacturers in this document does not constitute an official endorsement of such products or manufacturers, either expressed or implied, by the National Aeronautics and Space Administration.

INLET DISTORTION FOR AN F/A-18A AIRCRAFT DURING STEADY AERODYNAMIC CONDITIONS UP TO 60° ANGLE OF ATTACK

Kevin R. Walsh
NASA Dryden Flight Research Center
Edwards, California

Andrew J. Yuhas
Analytical Services and Materials
Hampton, Virginia

John G. Williams and William G. Steenken
General Electric Aircraft Engines
Evendale, Ohio

ABSTRACT

The effects of high-angle-of-attack flight on aircraft inlet aerodynamic characteristics were investigated at NASA Dryden Flight Research Center, Edwards, California, as part of NASA's High Alpha Technology Program. The highly instrumented F/A-18A High Alpha Research Vehicle was used for this research. A newly designed inlet total-pressure rake was installed in front of the starboard F404-GE-400 engine to measure inlet recovery and distortion characteristics. One objective was to determine inlet total-pressure characteristics at steady high-angle-of-attack conditions. Other objectives include assessing whether significant differences exist in inlet distortion between rapid angle-of-attack maneuvers and corresponding steady aerodynamic conditions, assessing inlet characteristics during aircraft departures, providing data for developing and verifying computational fluid dynamic codes, and calculating engine airflow using five methods. This paper addresses the first objective by summarizing results of 79 flight maneuvers at steady aerodynamic conditions, ranging from –10° to 60° angle of attack and from –8° to 11° angle of sideslip at Mach 0.3 and 0.4. These data and the associated database have been rigorously validated to establish a foundation for understanding inlet characteristics at high angle of attack.

NOMENCLATURE

A8R	right exhaust nozzle throat area, percent
AIP	aerodynamic interface plane
ALF	aft looking forward
AOA	angle of attack, deg

AOSS	angle of sideslip, deg
ARP	Aerospace Recommended Practice
CFD	computational fluid dynamics
C_p	pressure coefficient
C_p*	pressure coefficient corresponding to local speed of sound
DFRC	NASA Dryden Flight Research Center, Edwards, California
DP/PC	circumferential distortion descriptor
DP/PR	radial distortion descriptor
F/A	fighter-attack aircraft
FS	fuselage station
FVG	fan vane guide position, deg
G^*	power spectrum density function, $psi^2/psi^2/Hz$
GEAE	General Electric Aircraft Engines, Evendale, Ohio
HAP	HARV analysis program
HARV	High Alpha Research Vehicle
HATP	High Alpha Technology Program
HPC	high-pressure compressor
HPL	pressure altitude, ft
HPVG	compressor vane guide position, deg
LEX	leading-edge extension
LPC	low-pressure compressor
LPT	low-pressure turbine
m	number of data samples
MIL-STD	military standard
n	number of total pressure probes
N1SR	right fan rotor speed, rpm
N2SR	right compressor rotor speed, rpm
P6REF	augmentor static pressure used as reference source for PS6 and PS7 pressures, psia
PAV	face average total pressure at the AIP, psia
PCM	pulse code modulation
PLAR	right engine throttle position, deg
PMIN	minimum total pressure at the AIP, psia
PRBAYC	right engine-bay pressure used as reference source for PSE and PTE pressures, psia

PS0	free-stream static pressure, psfd
PS211	fan exit static pressure at 300-deg position, psia
PS212	fan exit static pressure at 120-deg position, psia
PS3R	combustor static pressure, psia
PS6 (3)	augmentor inlet static pressures, psid
PS7 (4)	nozzle inlet static pressures, psid
PSB1	combustor static pressure at 270-deg position, psia
PSB2	combustor static pressure at 90-deg position, psia
PSD	power spectral density function, $psi^2/psi^2/Hz$
PSE	low-response inlet surface static pressure, psid
PSE8	low-response static pressures at the AIP
psfd	pounds per square foot, differential pressure
PSFUELI	inlet fuel pressure of main fuel control, psia
PSFUELO	outlet fuel pressure of main fuel control, psia
PSI	Pressure Systems Incorporated, Hampton, Virginia
psia	pounds per square inch, absolute pressure
psid	pounds per square inch, differential pressure
PSK	high-response inlet surface static pressure, psia
PTE	low-response inlet total pressure, psia
PT0	free-stream total pressure, psia
PT56 (20)	right turbine discharge pressures, psia
PTK	high-response inlet total pressure, psia
PW (pk-pk)	peak-to-peak variance of the planar wave descriptor
QBAR	freestream dynamic pressure, lbf/ft^2
REC	inlet recovery value
rms	root-mean-squared
RTTM	real-time thrust methodology
SAE	Society of Automotive Engineers
sps	samples per second
T1R	right engine inlet temperature, °R
T1RRB	right engine inlet temperature with bias, °R
T56HR	right engine turbine exhaust gas temperature, °R

TT0	free-stream total temperature, °R
TU	inlet turbulence parameter
W1R	right engine corrected inlet airflow, lb/sec
WFABM	right engine main augmentor fuel flow, gal/min
WFABMT	fuel temperature of WFABM, °F
WFABP	right engine pilot augmentor fuel flow, gal/min
WFE	right engine combustor fuel flow, gal/min
WFEP	right engine combustor fuel flow, lb/h
WFET	fuel temperature of WFE, °F

INTRODUCTION

Inlet pressure distortion effects on the propulsion system at high angle of attack (AOA) during steady aerodynamic conditions, rapid aircraft maneuvers, and aircraft departures are not thoroughly understood. A team of NASA and industry researchers was formed as part of the NASA High Alpha Technology Program (HATP) to investigate inlet characteristics, inlet and engine compatibility, and prediction methodologies at high-AOA conditions. This effort addressed questions that have arisen during past aircraft development programs. These questions included the following subjects:

- At high-AOA, how do the inlet total-pressure characteristics, such as inlet recovery, circumferential and radial distortion, planar wave, and turbulence, behave as a function of angle of sideslip (AOSS) and Mach number?

- How do inlet distortion levels during rapid, high-AOA maneuvers compare with those at corresponding steady aerodynamic flight conditions?

- What are the characteristics of the inlet during aircraft departures? What factors lead to engine surges that have been experienced during aircraft departures? Are there any other significant factors beyond inlet-induced distortion which account for engine surges?

- Can computational fluid dynamics (CFD) technology be used to accurately predict inlet characteristics at high-AOA conditions?

- Are the engine airflow pumping characteristics affected at extreme maneuver conditions? What is the best method for measuring airflow in flight at these conditions?

To address each of these questions, mapping of inlet characteristics as a function of AOA, AOSS, and Mach number was conducted on the F/A-18A High Alpha Research Vehicle (HARV). The inlet data obtained at steady aerodynamic conditions formed the foundation for this inlet research effort.

The HARV aircraft, flown at the NASA Dryden Flight Research Center (DFRC), Edwards, California, provided the ideal platform for controlled exploration of inlet characteristics related to highly agile vehicles at full scale.[1] The thrust-vectoring vane system provided the ability to maintain steady, high-AOA conditions. The aircraft was highly instrumented, with emphasis on the region around and in the starboard inlet and engine. A newly developed, 40-probe total-pressure inlet rake was installed directly ahead of the engine.[2] Surface static-pressure transducers were installed at the inlet rake location and around the inlet lip. High-frequency-response instrumentation was installed to monitor engine operation and behavior. To maintain the quality of the high-response data, a series of specific instrumentation calibrations was performed on the ground and in flight during the course of the test program.

Flight test data were obtained during steady aerodynamic conditions, rapid changes in AOA and AOSS,[3] and aircraft departures.[4] These flight test data were also used to estimate engine airflow with clean and distorted flows[5] and to improve a CFD approach of predicting dynamic distortion.[6] The steady aerodynamic test matrix consisted of 79 conditions with the engine at maximum-corrected airflow. The majority of the flight data was acquired at Mach 0.3 and 0.4, with limited testing performed at Mach 0.6, 0.8, and 0.9. Special in-flight testing was performed to verify data repeatability. An exhaustive verification of the data processing and reduction system was completed before beginning the analyses.

A sophisticated data reduction program was developed by General Electric Aircraft Engines (GEAE), Evandale, Ohio, to perform all data quality and analysis calculations. These calculations included inlet characteristics, such as inlet recovery, circumferential and radial total-pressure distortion levels, and also planar wave and turbulence values. The program provided time-averaged and peak-pattern screening of the inlet characteristics. The distortion descriptors were calculated consistent with Society of Automotive Engineers (SAE), Aerospace Recommended Practice (ARP) 1420, and Aerospace Information Report (AIR) 1419 standards,[7,8] and established GEAE methodology.[9,10]

This paper summarizes the results of inlet data validation and inlet performance analysis for steady aerodynamic flight conditions. Inlet data repeatability is discussed first by showing inlet recovery pressure patterns and distortion levels at Mach 0.3, 30° AOA and 0° AOSS. A summary of the effect of AOA and AOSS on inlet recovery, turbulence levels, and peak dynamic circumferential and radial distortion is then presented for Mach 0.3 and 0.4. A summary of the effects of AOA and AOSS on the wall static pressures at the inlet exit for Mach 0.3 is shown. Lastly, a summary of the effects of AOA at 0° AOSS on the inlet cowl lip and duct surface pressures is presented.

AIRPLANE

The F/A-18A airplane is a twin-engine, single-place, multimission fighter/attack airplane with all-weather intercept and ground attack capability. The HARV is a preproduction model (aircraft no. 6) of the F/A-18A airplane which was modified with extensive instrumentation and multiaxis thrust-vectoring paddles (fig. 1). Thrust vectoring provided the HARV with the ability to fly at sustained aerodynamic conditions which exceed the capabilities of conventional aircraft. Wing

leading-edge extensions (LEX) were mounted on each side of the fuselage from the wing roots to just forward of the windshield.

PROPULSION SYSTEM

The F/A-18A propulsion system consists of two inlets and two General Electric F404-GE-400 turbofan engines with afterburner and thrust-vectoring paddles. The right-hand inlet and engine (ALF) were used for conducting inlet research.

Air Induction

Two inlets and inlet ducts make up the air induction system of the F/A-18 airplane. These inlets are side-fuselage-mounted with fixed geometry and a single 5° external compression ramp. The inlets are located approximately 25 ft aft of the aircraft nose under the LEX of the wing (fig. 1). Figure 2 shows a schematic of the air induction system, including key inlet dimensions. The inlets are located approximately 5 in. from the fuselage to avoid ingestion of the fuselage boundary layer. The fuselage boundary-layer flow is diverted upward and downward by a wedge-shaped diverter between the ramp and the fuselage.

The external and internal geometry of the inlet cowl lip was optimized for maneuvering in the subsonic, high-AOA region of the flight envelope. The lower and lower-inboard portions of the inlet lip were cut back and thickened to decrease the compressor-face distortion at extreme aircraft attitudes.

The length of the subsonic diffuser is approximately 13 ft. The diffuser length to engine-face diameter ratio is 5.3, which provides for a gradual transition from the inlet entrance to the engine face. The inlet entrance is offset from the engine centerline by 10 in. in the horizontal plane and 14 in. in the vertical plane. A pair of vortex generators were installed on the lower surface of the diffuser to prevent possible local flow separation in this area. References 11 and 12 provide detailed descriptions of the F/A-18A air induction system.

Engines

The F404-GE-400 is a low-bypass, twin-spool, axial-flow turbofan engine with afterburner. The 3-stage fan (low-pressure compressor) and 7-stage high-pressure compressor are each independently driven by a single-stage turbine. In the fan, the inlet guide vanes and the stators of the first stage are variable. In the high-pressure compressor, the inlet guide vanes and the first two stator stages are variable. These variable inlet guide vanes direct the inlet air at an optimum angle for efficient engine operation. The through-flow annular combustor uses atomizing fuel nozzles. The mixed-flow augmentor burns air from both the bypass and the high-pressure core in the afterburner

section. The engine control is an integrated system, using both hydromechanical and electronic control components. The sea level static military thrust of each engine is approximately 10,700 lbf, and the maximum afterburner thrust is approximately 16,000 lbf. The maximum corrected airflow through the engine is approximately 144 lb/sec.

Thrust-Vectoring Vane System

The thrust-vectoring vanes were mounted on the aircraft and positioned about the periphery of the engine, behind the nozzle exhaust. The corners of each vane were clipped to avoid interference with adjacent vanes at full deflection. Electrohydraulic actuators provided vane actuation.

The engines were modified to accommodate thrust-vectoring vane installation by removing the divergent section of the nozzle. The remaining convergent nozzle hardware was modified to maintain structural integrity. Reference 1 provides further details of the HARV thrust-vectoring vane system.

INSTRUMENTATION

The HARV inlet research objectives required accurate measurement of specific inlet, engine, and airdata parameters. These measurements needed to be recorded during steady aerodynamic flight conditions up to 60° AOA, rapid AOA maneuvers, and aircraft departures with possible engine surges. This section summarizes the instrumentation used for the HARV inlet research program. Table 1 summarizes the important pressure transducers that were used.

Table 1. Summary of inlet research transducers.

Description	Type	Range	Measurement sample rate, sps
High-response pressure transducers (PTKxy and PSKxy)	Absolute	0–20 psia	2143
Low-response pressure transducers (PTExy and PSExy)	Differential	±5 psid	67
Inlet reference pressure (PRBAYC)	Absolute	0.4–19 psia	67
Fan exit diagnostic pressures (PS211, PS212)	Absolute	0–50 psia	800

Aircraft and Engine

Aircraft instrumentation included accelerometers, rate gyros, surface position measurements, and airdata. Data monitored from the MIL-STD-1553 data bus included 226 flight control system,

21 airdata, 37 engine and aircraft diagnostic, and 32 inertial navigation system parameters. Two high-AOA flight research airdata systems consisting of swiveling pitot probes with conventional AOA and AOSS vanes were mounted on both wingtips.[13]

Both engines had basic instrumentation for monitoring engine operation and were equipped with a real-time thrust measurement (RTTM) system.[14] Figure 3 shows the right engine instrumentation. Additional flight test instrumentation was installed to measure guide vane positions, fan and compressor speeds, fuel flows, diagnostic pressures, and RTTM pressure measurements.

Inlet Rake

An innovative inlet total-pressure distortion measurement rake was developed for the A/B/C/D models of the F/A-18 airplane inlet by a team of NASA Dryden and GEAE personnel. Figure 4 shows the inlet rake installed at the aerodynamic interface plane (AIP) with the engine installed. The AIP is defined as the measurement plane between the inlet and the engine where inlet distortion and performance is determined. For the F/A-18, the AIP is located 4 in. in front of the bullet nose of the engine. The inlet rake consisted of a streamlined centerbody and eight aerodynamic rake legs. The rake legs were equally spaced, oriented 45° from each other starting at 9° counterclockwise off top center aft looking forward (ALF) for the right-hand inlet. Each rake leg consisted of five dual probes located at the centroids of five equal areas. The 40 dual probes measured high- and low-frequency-response total pressures. Figure 5 shows the rake orientation and nomenclature used to assign each pressure port. This inlet rake is fully described in references 2 and 15. The orientation of the rake was consistent with that used in previous F/A-18 inlet tests.[11]

The inlet rake probe configuration was designed to be insensitive to flow angularity, an important criterion when measuring total pressure in distorted flows. This configuration allowed the sensors to read true pressure levels of local airflow at yaw angles from ±25° and pitch angles from 15° to –25°, with positive angles being in the direction of the engine centerline. The blockage of total airflow at the AIP caused by inlet rake probes was 0.4 percent. The maximum airflow blockage caused by the rake structure was less than 8 percent, located 1.5 in. downstream of the AIP.

Inlet Low-Response Pressures

The low-frequency-response pressures (PSEs and PTEs) were measured using differential pressure transducers (ESP-320S BSL, Pressure Systems, Inc., Hampton, Virginia). To obtain absolute pressures, an accurately measured reference pressure was added to the differential pressures. The right-hand ALF engine-bay was selected as the reference pressure location.

Each differential transducer unit provided the measurement of 32 individual pressures. The units were thermally stabilized to minimize zero drift associated with temperature variations. This stabilization was accomplished by wrapping the transducer unit in a temperature-controlled thermal blanket. The differential pressure transducers were capable of in-flight calibrations. The

calibration system allowed for the reference-pressure pneumatic source to be supplied simultaneously to each side of the differential-pressure sensors. These data allowed for any change in the zero intercept of the calibration to be removed and thereby increase the overall accuracy of differential pressure measurements. In-flight calibrations were performed at straight and level conditions before initiating each set of flight research maneuvers.

Inlet High-Response Pressures

The high-frequency response pressures (PSKs and PTKs) were measured using individual temperature-compensated pressure transducers (XCS-27L-093-20A, Kulite Semiconductor Products Inc., Leona, New Jersey). Each transducer was mounted at the rake measurement ports in close proximity to the low-frequency response pressure probe. These transducers were selected, in part, because of their passive temperature compensation capability. This ability minimized any calibration drift which occurred because of changes in the thermal environment at the transducer sensor. To further increase the accuracy of the transducer measurement, a series of pressure calibrations were performed over the entire required pressure and temperature range, up to 20 psia and at 395, 425, 460, 535, and 610 °R. Along with the measured engine inlet temperature, these calibrations allowed any remaining zero thermal drift to be removed during postflight data processing. The flight calibrated, low-response pressure measurements were then used to remove any bias or drifting of the high response pressure measurements during steady aerodynamic flight conditions. This high-response transducer setup allowed for accurate measurement of total and static pressures during rapid aircraft maneuvers and departures. The sample rate of these transducers was configured to 2143 sps.

Inlet Wall Static Pressures

The inlet wall static pressure measurements surveyed the inlet, primarily at its entrance and exit. Twenty-eight low-response measurements and 14 high-response measurements were obtained using the same transducer setup as the inlet rake total pressures described in the sections on inlet low- and high-response pressures. Table 2 shows how the inlet wall static pressure measurement locations were distributed.

Table 2. Inlet wall static pressure probe distribution.

Location	Low-frequency response, PSE	High-frequency response, PSK
Inlet entrance	17	4
Inlet throat	2	2
Vortex generator	1	0
AIP	8	8

The low- and high-response tranducers were located about the aircraft fuselage station (FS) positions (0 FS is the aircraft nose tip location) (table 3). The curvature of the inlet entrance made exact fuselage station locations difficult to measure. At the inlet entrance an alternate method to define the fuselage station location was used to specify distance from the inlet tip. Arc measurements were obtained by placing a string alongside the differential pressure transducer locations at each clock position (0°, 90°, 180°, 225° ALF) and marking the position on the string. The 0° position is located at the top of the inlet. The tip probe locations (2A, 2C, 2E, 2F) were used as the 0 in. reference for each clock position. A positive length indicates that the port is located in the inlet, downstream of the inlet tip. A negative distance indicates that the port is outside of the inlet, downstream of the inlet tip.

Table 3. Locations of the low- and high-frequency-response static pressure measurements.

Low-pressure transducer static pressures			
Parameter identification	Fuselage station, in.	Angular position, deg†	Distance from inlet cowl lip highlight, in.
PSER1A	FS411.5	0° (outer skin)	–0.750
PSER2A	FS411	0° (lip tip)	0.0
PSER3A	FS411.5	0° (inner skin)	0.938
PSER4A	FS412.5	0° (inner skin)	1.875
PSER1C	FS411.25	90° (outer skin)	–0.813
PSER2C	FS410.75	90° (lip tip)	0.0
PSER3C	FS411.25	90° (inner skin)	0.688
PSER1E	FS415.5	180° (outer skin)	–0.563
PSER2E	FS415	180° (lip tip)	0.0
PSER3E	FS415.5	180° (inner skin)	1.063
PSER4E	FS416	180° (inner skin)	1.750
PSER5E	FS422	180° (inner skin)	7.750
PSER6E	FS426	180° (by throat)	11.750
PSER7E	FS495	180° (by vortex generator)	89.0
PSER1F	FS415.5	225° (outer skin)	–0.813
PSER2F	FS415	225° (lip tip)	0.0
PSER3F	FS415.5	225° (inner skin)	1.000
PSER4F	FS416.25	225° (inner skin)	2.188
PSER5F	FS418	225° (inner skin)	4.250
PSER6F	FS426	225° (by throat)	12.313
PSER8A	FS551	12.25° (AIP)	140.0
PSER8B	FS551	58.75° (AIP)	140.0
PSER8C	FS551	97.50° (AIP)	140.0
PSER8D	FS551	144° (AIP)	140.0
PSER8E	FS551	189° (AIP)	140.0

Table 3. Concluded.

Parameter identification	Fuselage station, in.	Angular position, deg†	Distance from inlet cowl lip highlight, in.
PSER8F	FS551	234° (AIP)	140.0
PSER8G	FS551	283° (AIP)	140.0
PSER8H	FS551	323° (AIP)	140.0
High-pressure transducer static pressures			
PSKR2A	FS411	3° (lip tip)	0.0
PSKR2C	FS410.75	93° (lip tip)	0.0
PSKR2E	FS415	183° (lip tip)	0.0
PSKR2F	FS426	183° (by throat)	11.75
PSKR6E	FS415	228° (lip tip)	0.0
PSKR6F	FS426	228° (by throat)	12.31
PSKR8A	FS551	9.25° (AIP)	140.0
PSKR8B	FS551	55.75° (AIP)	140.0
PSKR8C	FS551	94.5° (AIP)	140.0
PSKR8D	FS551	141° (AIP)	140.0
PSKR8E	FS551	186° (AIP)	140.0
PSKR8F	FS551	231° (AIP)	140.0
PSKR8G	FS551	280° (AIP)	140.0
PSKR8H	FS551	320° (AIP)	140.0

†0° = Top, clockwise, ALF.

Figure 6 shows the inlet wall static locations about the inlet entrance. The low-response wall static positions at the AIP were equally spaced between each rake and were in the same plane as the rake probe tips. High-response positions were approximately clocked 0.5 in. (3°) clockwise and ALF from the corresponding low-pressure transducer locations.

Data Acquisition and Reduction

Data acquisition for the HARV inlet program used three pulse code modulation (PCM) systems. Two PCM systems telemetered aircraft and engine data to ground-based computers. The third recorded inlet specific data onboard the aircraft. The high-response absolute-pressure transducers had an onboard antialiasing filter applied to the measurement signals. The onboard, six-pole, low-pass analog filter provided a nominal cutoff frequency (–3 dB point) of 400 Hz with a 36 dB per octave rolloff. Additional filtering was applied to the signals during data reduction. This digital filter used a 9-scan rolling window average providing a cutoff frequency equivalent to 100 Hz which is consistent with the F404-GE-400 engine response to effects of dynamic distortion.

To synchronize the three PCM systems, an embedded time-code was inserted into each data stream. The telemetered data were synchronized with the onboard recorded data at the fastest sample rate, 2143 sps. Data obtained for each test condition were reduced and processed through special data quality and analysis computer programs to assure high quality data. The data synchronization, pressure data corrections, data quality checks, and analysis were conducted postflight.

Data Quality Assurance

A quality assurance software program was developed to review and verify the validity of HARV inlet data. For each research maneuver, the average, maximum, minimum, and rms values were calculated for all parameters. An output summary file provided averages and ratios of the high- and low-response pressure data, and also of simple inlet flow quality descriptors.

Data Tolerance Levels

The quality assurance software validated data sets by comparing the current value of each input parameter with its previous value to determine whether the latter exceeded user-defined tolerances. These tolerances were defined by either a percentage or an absolute change in the value. The quality assurance software replaced any out-of-tolerance data by holding the last validated value. Any out-of-tolerance data were investigated to determine whether tolerance limits required modification. The software also calculated the average, maximum, minimum, and root mean square (rms) values over the entire input file for all parameters.

Probe Substitution

For the 40 rake total and 8 wall static high-response pressures measured at the AIP, any transducer that was known to be inoperative was substituted. The substitution procedure was based on information from adjacent circumferential pressure measurement locations.

DATA ANALYSIS

The HARV Analysis Program (HAP) was specifically developed to analyze HARV inlet data. Two output files were generated for database storage. One contained the computed information for each scan of the data record. The other contained a summary of the time-averaged dynamic and peak parameter information obtained from each flight test maneuver.

Time-averaged values were calculated for all input parameters. Inlet and engine pressure distortion indices were computed to describe the flow field characteristics. Output from the HAP consisted of circumferential and radial elements of distortion descriptors displayed in tabular and graphical form. Isocontour plots of the AIP pressures were graphically displayed to correspond to specified peak distortion descriptors. This HAP data also provided information to assess the influence of the descriptors on the engine stall line.

Appendix A contains the procedures for computing the parameters used to describe inlet airflow quality. These procedures reflect a history of successful correlation of inlet distortion effects for the F404 engine and other military and commercial engines. These procedures are based on industry standard guidelines[3,4] and are consistent with GE methodology.[5] The inlet total pressure and flow stability descriptors described are based on the F404-GE-400 Engine Model Specification.[6]

FLIGHT TEST DESCRIPTION

A matrix of aerodynamic flight conditions was required to evaluate the inlet research objectives. These conditions consisted of steady attitudes of AOA and AOSS, positive and negative sweeps of AOA, and aircraft departures. All testing was performed between military (maximum dry) and maximum afterburning power settings to maintain a constant engine airflow of approximately 144 lb/sec. When on flight condition, the power setting was held steady while research data were recorded. The maneuvers at steady aerodynamic conditions were conducted at Mach 0.3 and 0.4 and from an altitude of 20,000 to 35,000 ft. Figure 7 summarizes the matrix of inlet data obtained during steady aerodynamic conditions for a given AOA, AOSS, and Mach number.

In-Flight Calibrations

During flight, calibrations of the inlet rake and duct, low- and high-response pressure transducers (PTE, PTK, PSE, and PTE) were performed prior to a series of steady aerodynamic flight maneuvers. The calibration required constant altitude and airspeed for 15 sec. The calibrations were conducted in two steps. The PTE and PSE transducers were calibrated at their zero differential pressure condition by applying the reference pressure to both sides of the transducer sensing element for 10 sec. Immediately following this calibration, 5 sec of PTK and PSK transducer calibration was obtained. The aircraft was required to maintain steady aerodynamic flight conditions (airspeed, AOA, AOSS, and right engine military power setting) during this interval. These PTK and PSK transducer calibrations consisted of comparing the time-averaged pressure levels of the high-response measurements (PTK and PSK) with their corresponding low-response measurements (PTE, PSE). Because of flight constraints, the pilot typically performed this calibration in a shallow climb.

Steady Aerodynamic Conditions

The criterion for a successful maneuver was that the flight condition tolerances be maintained. The length of recorded data for each maneuver was established to be 6 sec; however, because of aircraft maneuver limitations, shorter data records were obtained at the more extreme aerodynamic conditions. To help assure the consistency of the data, the tolerance for Mach number during every maneuver was ±0.01. The tolerance for AOA and AOSS was ±1.0°. For the ±10° AOSS maneuvers, it was not possible for the airplane to maintain a 10° or –10° AOSS condition. As a result, the maximum sustainable AOSS condition was used.

RESULTS AND DISCUSSION

This section presents a summary of inlet data obtained during steady aerodynamic flight conditions. Inlet data repeatability is discussed first by showing inlet recovery pressure patterns and distortion levels at Mach 0.3, 30° AOA, and 0° AOSS. A summary of the effect of AOA, AOSS, and Mach number on inlet recovery, turbulence levels, peak dynamic circumferential and radial distortion is presented for Mach 0.3 and 0.4. A summary of the effects of AOA and AOSS on the wall static pressures at the AIP at Mach 0.3 is shown. Lastly, a summary of the effects of AOA, at 0° AOSS, on the inlet cowl lip and duct surface pressures is presented.

All inlet pressure data presented here incorporate the in-flight calibrations and postflight instrumentation bias corrections. These calibrations and corrections were necessary for obtaining accurate and repeatable data.

Data Repeatability (Mach 0.3, 30° AOA, 0° AOSS)

To evaluate data repeatability, time-averaged total pressure patterns (or contours) were obtained using high response (PTK) pressure measurements. Four of the eleven test points at Mach 0.3, 30° AOA, and 0° AOSS were compared. The contour lines represent a deviation from face average pressure. The four test points spanned 31 flights and 2 months.

Figure 8 shows the total pressure patterns for the four test points. All four pattern profiles are nearly identical. Values of inlet recovery, turbulence, and maximum dynamic distortion are also nearly identical. A low-pressure area is protruding from the lower, inboard wall. This area is indicated by the contour line labeled –6, which shows the percent decrease in pressure relative to the face average pressure. The circumferential and radial distortion descriptors, DP/PC and DP/PR, are nearly identical for the four steady aerodynamic conditions. Although not shown here, the distortion characteristics of the other Mach 0.3, 30° AOA, and 0° AOSS conditions are also very similar. These data indicate that the high-response PTK pressures have excellent repeatability.

Inlet Performance at Mach 0.3 and 0.4

For figures 9–13, the data points represent time-averaged values for inlet recovery, turbulence, and peak distortion descriptor values as a function of AOA and AOSS. A solid symbol indicates that only one set of time-averaged data was obtained for the target AOA condition. The open symbols and the ‘x’ indicate that multiple data sets were obtained at the target AOA condition. All data shown in figures 9(a), 10(a), 11(a), 12(a), and 13(a) were obtained at Mach 0.3 and are shown in table 4. Figures 9(b), 10(b), 11(b), 12(b), and 13(b) show data obtained at Mach 0.4 and are shown in table 5. Positive AOSS indicates that the aircraft is pointing nose-left. This orientation is windward for the right-hand inlet. Conversely, negative AOSS describes a nose-right condition. This orientation is leeward for the right-hand inlet.

Table 4. Inlet performance at Mach 0.3.

Flight/ Test Point	Flight Conditions						Inlet data				
	Mach	AOA	AOSS	HPL	PTO	TTO	Inlet Recovery	Turbulence	DP/PC max	DP/PR max	Planar Wave
		deg	deg	ft	psia	°R	(PTE)	(rms)	(based on PTK + bias)		(pk-pk)
215/08b	0.30	-8.6	–1.4	22924	6.3549	452.9	0.9618	0.010	0.094	0.046	0.0137
230/6b3	0.31	3.6	0.9	24034	6.0779	448.0	0.9731	0.005	0.051	0.056	0.0104
234/06b	0.31	11.0	–7.9	22537	6.4734	466.3	0.9679	0.007	0.088	0.052	0.0088
216/14d2	0.30	10.7	–5.6	22509	6.4765	458.0	0.9686	0.006	0.084	0.052	0.0098
211/4b3	0.31	9.9	0.8	22638	6.4494	463.4	0.9741	0.005	0.065	0.059	0.0091
230/12b1	0.32	9.4	0.8	21834	6.7122	458.0	0.9749	0.005	0.063	0.056	0.0072
216/14b	0.31	9.4	6.2	21086	6.9073	461.4	0.9760	0.004	0.060	0.054	0.0094
216/14c	0.30	9.3	8.3	22016	6.6051	458.0	0.9731	0.005	0.049	0.057	0.0100
212/08b	0.30	20.1	0.4	22926	6.3464	462.5	0.9765	0.005	0.053	0.046	0.0090
211/25c	0.31	30.4	–8.3	25603	5.6851	452.6	0.9605	0.010	0.098	0.046	0.0142
215/10c	0.28	30.8	–7.8	22828	6.3274	452.6	0.9619	0.009	0.095	0.044	0.0123
215/10b	0.29	30.0	–3.4	23660	6.1366	449.3	0.9678	0.009	0.090	0.046	0.0131
211/24c2	0.31	30.5	–2.8	27095	5.2313	446.9	0.9683	0.009	0.097	0.046	0.0162
230/02b	0.31	31.0	–0.3	25623	5.6686	441.8	0.9701	0.008	0.090	0.048	0.0128
238/26b	0.30	29.8	–0.2	22132	6.5644	447.2	0.9709	0.007	0.083	0.045	0.0121
213/02b	0.30	30.1	0.2	25916	5.5700	452.6	0.9695	0.007	0.082	0.047	0.0119
234/02b	0.29	29.6	0.3	21584	6.7043	466.4	0.9715	0.007	0.076	0.048	0.0105
232/02b	0.29	29.9	0.3	25052	5.7791	437.1	0.9697	0.007	0.085	0.046	0.0135
211/02b	0.30	30.0	0.3	25405	5.7008	452.7	0.9712	0.007	0.083	0.045	0.0132
241/26b	0.30	30.1	0.3	25118	5.7706	454.4	0.9698	0.007	0.082	0.048	0.0119
212/02b	0.30	29.8	0.4	23176	6.2721	463.4	0.9699	0.007	0.080	0.047	0.0116
215/02b	0.30	29.9	0.6	25782	5.6202	443.0	0.9702	0.007	0.084	0.046	0.0129
216/02b	0.31	29.9	0.9	24828	5.8660	446.4	0.9705	0.007	0.081	0.046	0.0119
214/02b	0.30	29.9	1.0	26301	5.4911	440.6	0.9702	0.007	0.084	0.046	0.0111
211/24b	0.30	29.7	3.5	24226	6.0026	456.2	0.9708	0.006	0.065	0.047	0.0110
215/10d	0.31	29.0	5.0	25972	5.5870	440.8	0.9719	0.006	0.059	0.051	0.0118
211/25b	0.29	30.1	6.4	23818	6.0931	458.1	0.9701	0.007	0.066	0.050	0.0129
230/02c	0.31	31.0	8.8	24490	5.9476	445.4	0.9683	0.007	0.074	0.056	0.0120
215/10e	0.31	28.6	10.8	25294	5.7546	444.0	0.9697	0.007	0.070	0.054	0.0124
247/08b	0.29	37.8	4.0	21533	6.7236	457.3	0.9610	0.009	0.102	0.059	0.0120
212/09b	0.30	39.6	0.3	23645	6.1617	461.2	0.9599	0.010	0.109	0.051	0.0140
247/08d	0.29	40.3	–3.5	21658	6.6758	459.9	0.9567	0.010	0.113	0.053	0.0148
232/03d1	0.29	49.7	–4.4	24593	5.8809	431.3	0.9293	0.018	0.152	0.073	0.0293
232/3d2	0.29	48.9	–3.7	21426	6.7498	443.7	0.9407	0.014	0.128	0.062	0.0174
242/13c	0.30	50.6	–3.6	23595	6.1583	453.8	0.9250	0.019	0.154	0.081	0.0264
232/03c	0.29	50.3	–2.8	27064	5.2885	421.4	0.9297	0.018	0.147	0.075	0.0228
240/12c	0.30	49.4	–1.6	21622	6.7139	452.1	0.9394	0.016	0.137	0.066	0.0249
213/10b2	0.30	49.4	–0.1	26601	5.4110	446.1	0.9380	0.016	0.126	0.067	0.0217
231/3b2	0.30	49.3	0.7	25109	5.7816	442.5	0.9402	0.015	0.129	0.067	0.0279
232/03b	0.30	49.7	1.5	24676	5.8916	432.6	0.9445	0.013	0.123	0.063	0.0197
240/12b	0.30	48.9	2.9	24086	6.0485	452.7	0.9456	0.014	0.110	0.062	0.0202
240/13b	0.31	49.2	3.1	24162	6.0532	450.5	0.9450	0.015	0.130	0.068	0.0252
231/3c2	0.30	49.1	3.4	23448	6.2207	447.7	0.9495	0.012	0.113	0.064	0.0173
231/03d	0.30	48.5	5.2	19730	7.2636	462.4	0.9503	0.012	0.110	0.059	0.0155
247/6b2	0.30	56.6	–2.2	24439	5.9432	448.1	0.9118	0.019	0.163	0.081	0.0227
243/29c	0.32	59.1	–2.2	27126	5.3336	439.7	0.8999	0.023	0.188	0.094	0.0270
247/6b1	0.32	59.1	–0.3	26904	5.3825	437.0	0.9040	0.022	0.164	0.091	0.0305
247/6b3	0.31	60.0	1.3	31865	4.2867	416.9	0.9040	0.024	0.167	0.102	0.0287
232/05b	0.30	58.9	1.9	26855	5.3488	421.9	0.9140	0.021	0.152	0.087	0.0231
242/17b1	0.30	59.1	1.9	28658	4.9404	433.9	0.9093	0.022	0.160	0.087	0.0272
242/16b	0.30	59.0	2.6	22229	6.5327	460.1	0.9147	0.019	0.141	0.078	0.0249
212/05b	0.30	59.0	2.7	25670	5.6384	448.4	0.9139	0.021	0.149	0.081	0.0284
243/16b	0.30	59.0	3.0	22501	6.4788	461.4	0.9144	0.019	0.144	0.075	0.0218
231/04b	0.31	59.2	3.5	26076	5.5514	435.4	0.9145	0.021	0.162	0.082	0.0231

Table 5. Inlet performance at Mach 0.4.

Flight/ Test Point	Flight Conditions						Inlet data				
	Mach	AOA	AOSS	HPL	PTO	TTO	Inlet Recovery	Turbulence	DP/PC max	DP/PR max	Planar Wave
		deg	deg	ft	psia	°R	(PTE)	(rms)	(based on PTK + bias)		(pk-pk)
215/09b	0.41	–10.3	0.2	24363	6.2847	453.7	0.9590	0.010	0.111	0.028	0.0159
230/07b	0.40	3.7	0.4	22653	6.7337	458.1	0.9776	0.005	0.043	0.055	0.0085
234/07c	0.41	9.3	6.8	22133	6.9360	468.9	0.9822	0.004	0.051	0.055	0.0066
234/07b	0.40	9.4	4.9	22099	6.8981	468.9	0.9815	0.004	0.047	0.055	0.0070
213/13b	0.39	9.9	0.6	22282	6.8125	468.9	0.9770	0.004	0.071	0.054	0.0078
234/07d	0.40	10.4	–4.7	21559	7.0655	474.3	0.9715	0.005	0.081	0.055	0.0083
234/07e	0.41	11.0	–5.9	22964	6.6691	468.9	0.9677	0.006	0.094	0.050	0.0088
213/14b	0.40	19.7	0.4	32134	4.4217	429.9	0.9786	0.005	0.055	0.051	0.0084
216/11c	0.42	27.2	7.5	28986	5.1683	429.1	0.9780	0.005	0.056	0.050	0.0108
231/08b	0.40	31.3	–7.6	25843	5.8663	442.8	0.9560	0.012	0.121	0.056	0.0245
216/11d2	0.41	29.5	–3.8	28470	5.2565	430.6	0.9673	0.009	0.100	0.055	0.0142
231/19b	0.40	29.4	–0.1	28182	5.2883	437.1	0.9740	0.007	0.067	0.051	0.0113
231/05b	0.41	29.0	0.0	32536	4.3580	417.4	0.9734	0.007	0.070	0.051	0.0113
213/15b	0.41	29.9	0.2	35287	3.8205	414.6	0.9747	0.007	0.066	0.051	0.0123
216/11b	0.39	29.3	3.5	32229	4.3654	414.0	0.9761	0.006	0.065	0.049	0.0121
243/25a1	0.40	38.3	4.1	30634	4.7248	432.1	0.9654	0.010	0.109	0.057	0.0177
241/10b	0.40	37.7	4.5	29065	5.0855	439.1	0.9681	0.010	0.096	0.057	0.0156
243/25c1	0.40	40.1	–4.5	34068	4.0367	414.2	0.9529	0.013	0.132	0.061	0.0237
241/10c	0.39	39.0	–4.0	28141	5.2741	441.6	0.9556	0.013	0.137	0.058	0.0179
214/2ab3	0.40	39.2	–0.3	36178	3.6499	403.2	0.9620	0.012	0.112	0.058	0.0177
233/04b	0.40	39.8	0.0	32800	4.2887	413.0	0.9618	0.011	0.112	0.059	0.0163
234/08b	0.40	38.9	1.2	33550	4.1332	415.0	0.9666	0.011	0.103	0.058	0.0164
235/08c	0.39	39.2	3.5	31165	4.6021	424.3	0.9665	0.011	0.101	0.057	0.0155

Inlet Recovery

Figures 9(a) and 9(b) show the effect of AOA and AOSS on inlet pressure recovery. An inlet recovery value of 1.0 indicates that the total pressure at the AIP is equal to the free-stream total pressure. This is the ideal value and indicates 100-percent pressure recovery at the AIP. Negative AOSS have an obvious detrimental effect on inlet recovery for all AOA at Mach 0.3 and 0.4. As AOA increases, the detrimental effect of AOSS becomes increasingly pronounced. Pressure recovery remains constant at approximately 97 percent from 4° to 30° AOA. At increases above 30°, the loss in pressure recovery becomes more sensitive to AOA. At Mach 0.3, 60° AOA, 0° AOSS, the pressure recovery is less than 91 percent (fig. 9(a)). At Mach 0.4, –10° AOA, pressure recovery levels are less than the recovery at 4° to 40° AOA and 0° AOSS (fig. 9(b)). Inlet recovery levels are highest in the 4° to 20° AOA range.

Turbulence

Figure 10 shows the effect of AOA and AOSS on turbulence levels. The detrimental effects of AOA and AOSS on turbulence are similar to those shown for inlet recovery. Comparing figure 9 with figure 10 shows that inlet recovery decreases as the flow turbulence increases. Going from nose-left to nose-right (positive to negative AOSS) increases turbulence. This AOSS trend is slightly more pronounced at Mach 0.4 than at Mach 0.3. The turbulence level at Mach 0.3 is approximately 0.005 from 4° to 20° AOA. The turbulence level begins to increase above 20° AOA. At 60° AOA, turbulence has increased to 0.022. At Mach 0.4, the turbulence level at –10° AOA is close to that at 40° AOA. Turbulence levels are lowest in the 4° to 20° AOA range.

Peak Dynamic Circumferential Distortion

Figure 11 shows the affect of AOA and AOSS on the peak dynamic circumferential distortion. As a function of AOA, these trends are similar to those of turbulence. The pronounced affect of AOSS is evident for all AOA at Mach 0.3 and 0.4. As the aircraft moves more nose-left (positive AOSS), the peak dynamic circumferential distortion decreases. From 4° to 30° AOA, this distortion increases slightly; above 30° AOA, it increases rapidly. For Mach 0.3, this distortion doubles from approximately 0.08 at 30° AOA to 0.17 at 60° AOA. At Mach 0.4 and 0° AOSS, decreasing AOA from 4° to –10° increases the peak dynamic circumferential distortion from 0.04 to 0.11. Peak dynamic circumferential distortion levels are lowest in the 4° to 20° AOA range.

Peak Dynamic Radial Distortion

Figure 12 shows that AOA and AOSS have little affect on peak dynamic radial distortion up to 40° AOA. At Mach 0.3, the minimum value of peak dynamic radial distortion was obtained at 30° AOA (fig. 12(a)). Increasing AOA from 40° to 60° causes the peak radial distortion to increase rapidly. Increasing AOA to 50° and 60° also increases the sensitivity to AOSS, similar to the AOSS effect previously discussed in this section. At Mach 0.4 and from 4° to 30° AOA, the peak radial distortion level is nearly constant at approximately 0.055 (fig. 12(b)). At –10° AOA, the peak radial distortion decreases to approximately 0.03. This trend is the opposite of the one obtained for the circumferential distortion data.

Peak-to-Peak Planar Wave

Figure 13 shows the peak-to-peak variance of the planar wave descriptor. Effects of AOA and AOSS on the peak-to-peak values of a planar wave are similar to the trends described for turbulence and distortion descriptor data. As AOA increases, variability increases for a given AOSS. For instance at Mach 0.4, 30° AOA, –7.5° AOSS, a higher peak-to-peak value of nearly 0.024 was obtained, compared with 0.011 at the other 30° AOA points (fig. 13(b)). The peak-to-peak planar wave levels are lowest in the 4° to 20° AOA range. The planar wave values at these high-power conditions were extremely low.

AIP Total Pressure Characteristics at Mach 0.3

Figures 14 to 16 show time histories of the maneuver flight conditions, isocontours of the time-averaged PTE pressures, and time histories and power spectral density function(s) (PSD) of the PTK inlet recoveries at locations 2A, 2D, 6A, and 6D. These locations were chosen to show a cross section of the variation in inlet recovery, turbulence levels, and PSD’s at the AIP. The contours are viewed from an ALF perspective.

10° AOA and 0° AOSS

Figure 14 shows the AIP total pressure characteristics and maneuver description for 10° AOA, 0° AOSS, and Mach 0.3. Time histories of Mach number, AOA, AOSS, and altitude are shown in figure 14(a). Figure 14(b) shows isocontours of time-averaged PTE total pressures. The majority

of the pattern is uniform with a small low-pressure region developing in the upper inboard region. The probe locations 2A, 2D, 6D, and 6A are highlighted as a reference for the PTK inlet recovery time histories (fig. 14(c)) and PSD's (fig. 14(d)). Probe locations 2D and 6D are in the high-pressure region (2 percent) and 2A and 6A are in a low-pressure region (–4 percent). This can also be seen in the PTK inlet recovery time histories (fig. 14(c)). The 2D and 6D locations are near 100 percent recovery; whereas, locations 2A and 6A are between 90-percent and 93-percent recovery. The very low activity of the time histories at locations 2D and 6D exhibit significantly reduced turbulence in comparison with locations 2A and 6A. The turbulence values (TU) are shown in figure 14(d).

Figure 14(d) shows PSD's corresponding to the figure 14(c) time histories. At locations 2D and 6D, a frequency peak can be seen at approximately 215 Hz. This frequency is equivalent to the 1-per-revolution blade passage frequency of the fan. Peaks can be seen at these locations against the low-turbulent airflow background. The 1-per-revolution frequency is not seen at locations 2A and 6A because of increased background airflow turbulence levels.

30° AOA and 0° AOSS

Figure 15 shows the effect of increasing AOA to 30° on the AIP total pressure characteristics. Time histories of the maneuver aerodynamic conditions are shown in figure 15(a). The isocontours of the time-averaged PTE pressures are shown in figure 15(b). Note the change in pattern from 10° AOA. The lowest pressure region is now exhibited in the lower inboard region. The high-pressure region is predominately in the upper and outboard regions of the inlet. Note the increase in the circumferential distortion descriptor DP/PC (0.061 at 30° AOA versus 0.045 at 10° AOA) and the decrease in the radial distortion descriptor DP/PR (0.037 at 30° AOA versus 0.048 at 10° AOA). The probe locations 2A, 2D, 6D, and 6A are highlighted as described in the "10° AOA and 0° AOSS" section.

Figure 15(c) shows time histories of the PTK inlet recoveries for highlighted probe locations. Location 6D now shows lower inlet recovery and higher turbulence when compared with 10° AOA. This corresponds to figure 15(b) where location 6D is in the low-pressure (–2 percent) region. Location 2D remains in the high-pressure region where inlet recovery is nearly 100 percent, and turbulence is low in comparison with the other locations. Turbulence at location 2D is slightly greater at 30° AOA than at 10° AOA.

Figure 15(d) shows PSD's of the figure 15(c) time histories. A 1-per-revolution frequency (215 Hz) can best be seen at location 2D. Turbulence at location 2A has increased enough to mask the 1-per-revolution frequency. At location 2D, and to a lesser extent location 2A, another frequency peak appears at approximately 55 Hz. The cause of this peak is currently unknown.

60° AOA and 0° AOSS

Figure 16 shows the effect of increasing AOA to 60° on the AIP total pressure characteristics. Time histories of figure 16(a) show increased variation in the aerodynamic conditions while trying to maintain 60° AOA. The flight condition tolerances could only be met for 4 sec. Isocontours, of the time-averaged PTE pressures show a pronounced pressure gradient across the face of the inlet

(fig. 16(b)). The low-pressure region occupies the inboard half of the inlet face and extends along the top and bottom outboard walls. The maximum low-pressure region (–10 percent) is along the mid-inboard wall; whereas, the maximum positive pressure region is an island about locations 3C and 3D. The circumferential distortion descriptor, DP/PC, increased to 0.103, and the radial distortion descriptor, DP/PR, increased to 0.057.

Time histories of the inlet recoveries of locations 2A, 2D, 6A and 6D are shown in figure 16(c). All time histories show the increase in turbulence level at 60° AOA. The inlet recovery ranges from approximately 80 percent at location 6A to approximately 96 percent at location 2D.

The PSD's from the PTK-recovery time histories have elevated energy levels across the frequency range (fig. 16(d)). These elevated levels mask out the frequency peaks that were obtained at AOA conditions of 30° and below.

Matrix of AIP Total Pressure Contours

The effects of high-AOA conditions on the inlet are vividly shown by the series of total-pressure contour patterns in figure 17. These patterns are based on time-averaged inlet rake measurements and summarize the AIP total pressure patterns obtained for a range of aerodynamic conditions. The patterns are arranged in ascending order of AOA from –10° at the bottom to 60° at the top of the page. The AOSS sequence goes from negative (nose-right) to positive (nose-left) and from left-to-right respectively in the figure. The AOSS range is approximately –8.3° to 8.8° at 30° AOA. Increasing the AOA from 10° to 60° results in an increase in size of the local pressure deficit in the lower inboard region and exhibits a more pronounced pressure gradient across the engine face for all AOSS. Also at 30° AOA, the positive AOSS (nose-left) patterns are similar to the 0° AOSS patterns. The patterns for negative AOSS show the effect of the flow field off the leeward side of the vehicle. This AOSS effect is most obvious at 10° and 30° AOA where the change in AOSS is greatest. The low-pressure region encroaches further across the face of the engine, and the high-pressure center area decreases. Above 30° AOA, AOSS has decreased affect on the contour patterns. This decrease results from the fuselage forebody having progressively less influence on the flow entering the inlet. The characteristics of the contour pattern for the negative AOA case are significantly different from those at positive AOA. This difference is most likely caused by the airflow off the LEX and fuselage forebody entering the inlet.

AIP Wall Static Pressure Characteristics at Mach 0.3

To better understand the flow characteristics at the inlet entrance and subsequent downstream effects at the AIP, the inlet lip static pressures were evaluated. The effect of AOA and AOSS on the AIP wall static pressures is shown in figure 18. The PSE pressures were time averaged, referenced to the free-stream total pressure, and obtained at Mach 0.3. Figure 18(a) shows the wall static pressure locations with reference to the inlet rake. The angular position of 0° references the top of the inlet duct. The orientation of figure 18(a) is ALF.

The effect of AOA on PSEs at 0° AOSS is shown in figure 18(b). The angular position from 12° to 323° corresponds to static pressure locations 8A to 8H. Increasing AOA from 10° to 60°

causes the minimum pressure to rotate from the 189° position (location E) to the 234° position (location F). This correlates well with the rotation of the rake low-pressure region as AOA increases in figure 17. Figure 18(b) shows that by increasing AOA from 10° to 30°, a small decrease in pressure occurs at locations D, E, and F. Increasing AOA to 50° the pressure decreases markedly at all locations. As AOA increases to 60°, the pressure decreases between 3 to 5 percent for all locations compared with the 50° AOA data.

Figure 18(c) shows the affect of AOSS on the PSE pressures at 30° AOA. Increasing AOSS from 0° AOSS to a nose-left position of 8.8° shows little change in static pressures. As the airplane moves nose-right to an AOSS of –8.3°, the decrease in pressure is small with the minimum pressure at locations D and E. This minimum pressure correlates well with figure 17. The lowest pressure region of the rake total pressures, at 30° AOA and –8.3° AOSS, is near the base of rake leg 4. Leg 4 is between wall locations D and E.

Inlet Lip Surface Pressure Characteristics at Mach 0.3

Figure 19 shows the affect of AOA on inlet entrance pressure coefficients for 0° AOSS and Mach 0.3. Pressure coefficients at 10°, 30°, 50°, and 60° AOA are shown. These data are from the same maneuvers as those presented in figure 18. Figures 19(a)–19(d) show four rows (circumferential rows A, C, E, and F) of pressure coefficients as a function of the distance from the inlet tip in inches. Figure 6 shows close-ups of the inlet lip transducer locations. The vertical line on each of the figures at 0.0 in. represents the inlet tip. A positive distance from the inlet tip denotes transducer locations further downstream along the inner wall of the inlet duct. Negative distance denotes downstream locations along the outside wall of the inlet duct.

A pressure coefficient of 1.00 represents the stagnation point of the flow as it impinges on the inlet lip. The horizontal line across each of the data figures represents the pressure coefficient corresponding to the local speed of sound. At free-stream Mach 0.3, the pressure coefficient is –6.947. At this flight condition a pressure coefficient more negative than –6.947 indicates local supersonic flow.

Figure 19(a) shows pressure coefficients at the top of the inlet duct. At –0.75 in. on the outer skin the pressure coefficient is near 1.0 for all AOA. This location is in close proximity to the stagnation point of the airflow entering the inlet. At 0.938 in. inside of the inlet tip, the local flow becomes supersonic at all AOA’s except 60°. At 10° AOA and 0.938 in. inside of the inlet tip, the minimum pressure coefficient of –9.255 was obtained for the top of the inlet duct.

At the outboard side of the inlet duct, or at the 90° position (fig. 19(b)), the pressure coefficients exhibit trends similar to what is seen in figure 19(a) as AOA increases. Comparing the side of the duct with the top of the duct, the pressure coefficients at the inlet tip when at 50° and 60° AOA are slightly more negative than at the top of the duct for the same conditions. Only the 10° AOA point 0.688 in. inside from the inlet tip is clearly supersonic. At this AOA and location, the minimum pressure coefficient of –7.950 was obtained. The other AOA conditions were near to sonic conditions at this location.

Figure 19(c) shows pressure coefficients at the bottom of the duct. Additional rows of static pressure measurements are presented for the 7.75 in. and 11.75 in. locations downstream of the inlet tip. The 11.75 in. location is near the inlet throat. The variation in pressure coefficients as AOA increases for all rows is more significant at the bottom of the duct than at the top or outboard side of the inlet entrance. Only the 10° AOA condition shows stagnated flow 0.75 in. outside of the inlet tip. At higher than 10° AOA, the stagnation point moves more downstream on the outer surface of the inlet. From the inlet tip inward to the 1.75 in. row, the pressure coefficients indicate supersonic flow for all AOA conditions except 10°. At the 7.75 in. and 11.75 in. locations, the pressure coefficients are increasing, indicating improved pressure recovery as the airflow moves downstream in the inlet duct.

Figure 19(d) shows the pressure coefficients at the wing and cowl junction. The variation in pressure coefficients as AOA increases (from the inlet tip to the 2.188 in. location) is the greatest at the wing and cowl junction. Only the 10° AOA condition shows stagnated flow 0.75 in. outside of the inlet tip. From the inlet tip inward to the 4.25 in. location, the pressure coefficients indicate supersonic flow for all AOA conditions except 10° and from 30° at the inlet tip. At 60° AOA, the pressure coefficients at the inlet tip to the 4.25 in. location show a flat profile which signifies separated flow. This is the condition where separated flow is most apparent.

CONCLUSIONS

Flight tests of the F/A-18 HARV were conducted to study effects of steady-state and dynamic pressure phenomena on inlet performance during steady aerodynamic conditions. Aerodynamic interface plane (AIP) total pressures, inlet entrance, duct, and AIP wall static pressures were measured for aircraft Mach 0.3 and 0.4 at various angle of attack (AOA) and angle of sideslip (AOSS) conditions. Analysis of this database has yielded the following conclusions:

1. Pressure measurements obtained at 30° AOA, 0° AOSS showed consistent results over the course of the flight test program. The inlet total pressure contours and inlet distortion descriptors were repeatable. Consistent results during steady aerodynamic conditions are essential for providing confidence in the analysis of inlet distortion during rapid aircraft maneuvers. In-flight pressure calibrations and postflight instrumentation bias corrections were essential for obtaining accurate and repeatable results.

2. At 0° AOSS, increasing AOA from 0° to 20° had little effect on time averaged inlet recovery. As AOA increased to 30°, inlet recovery began to decrease. As AOA was increased from 30° to 60°, the loss in inlet recovery becomes more pronounced. The trend of the loss in inlet recovery at increasing AOA was similar to the trend of higher levels of turbulence and circumferential distortion at increasing AOA. The highest levels of inlet recovery occurred in the AOA range from 4° to 20° and coincided with the lowest turbulence and distortion levels.

3. At positive AOSS (nose-left aircraft position), the right-hand inlet was most efficient at all AOA. At 5° AOSS, the airflow has a more direct, streamlined path through the inlet with little fuselage interactions as compared to nose-right. By rotating the aircraft nose-right

(increasingly negative AOSS) while maintaining AOA, the inlet recovery, turbulence, and circumferential distortion descriptors were adversely affected. This adverse affect becomes more evident as AOA increases. The airflow becomes increasingly turbulent as a result of its interactions with the fuselage as evidenced by the separation of the inlet lip pressures.

4. The total pressure contour patterns show that increasing the AOA from 10° to 60° results in an increase in the size of the local pressure deficit in the lower inboard region and exhibits a more pronounced pressure gradient across the engine face for all AOSS. The positive AOSS (nose-left) patterns are similar to the 0° AOSS patterns. The patterns for negative AOSS show an adverse effect on the flow field off the leeward side of the vehicle. The characteristics of the contour pattern for negative AOA cases differs significantly from those of positive AOA. This difference is most likely caused by the airflow off the LEX and fuselage forebody entering the inlet.

5. At the top of the inlet duct, pressure coefficients obtained at all AOA conditions indicate stagnated flow near 0.75 in. outside of the inlet tip. Stagnated flow is also indicated at the side of the duct for all AOA except the 60° condition. For the bottom of the duct and the wing and cowl junction, only the 10° AOA condition shows stagnated flow 0.75 in. outside of the inlet tip. Supersonic flow is most evident at the bottom of the inlet duct and at the wing and cowl junction. Pressure coefficients from the inlet tip (0.0 in. location) to the 4.25 in. location indicate supersonic flow at all AOA's except for 10° AOA. As the airflow travels downstream, pressure recovery is apparent. At the wing and cowl junction, the flat pressure coefficient profile at 60° AOA indicates separated flow.

APPENDIX A
INLET FLOW DESCRIPTOR DEFINITIONS

For a given pattern of 40 total pressure measurements (8 rakes, 5 rings), the total pressure distortion descriptors are defined as follows:

Maximum Circumferential Distortion Descriptor - DP/PC max

This circumferential ring pressure distortion index is based on the calculation of $DP/PC_{ring\ i}$, where the subscript "ring i" refers to any of the five pressure rings.

The rings are counted in ascending order, outermost to innermost.

$$DP/PC_{ring\ i} = \{[PAV_{ring\ i} - PMIN_{ring\ i}] / PAV\} \text{ for rings } i = 1,5$$

where

$PAV_{ring\ i}$ is the area-averaged total pressure of ring i

$PMIN_{ring\ i}$ is the minimum total pressure in the largest low-pressure region in ring i

PAV is the area-averaged total pressure at the engine face

DP/PC max is defined as the largest of

$$0.5 * [DP/PC_{ring\ i} + DP/PC_{ring\ i+1}] \text{ for } i = 1,4$$

Maximum Radial Distortion Descriptor - DP/PR max

Similar to DP/PC, DP/PR is calculated for each of the five rings as follows:

$$DP/PC_{ring\ i} = [PAV - PAV_{ring\ i}] / PAV \text{ for rings } i = 1,5$$

where

PAV is the area-averaged total pressure over the complete face

$PAV_{ring\ i}$ is the area-averaged total pressure of ring i

If a DP/PR ring value is negative, it is assumed to be zero. DP/PR max is defined as the larger of $DP/PR_{ring\ 1}$ or $DP/PR_{ring\ 5}$. If DP/PR max is located in ring 1, the distortion is hub radial. If DP/PR max is located in ring 5, the distortion is tip radial.

Planar Wave Peak-to-Peak

The steadiness of the inlet recovery with time is quantified by the planar wave peak-to-peak parameter. First, the AIP average total pressure is computed at each time slice (PAV) and then averaged over a period of interest ($\overline{PAV}$):

$$PAV = 1/n \sum_{i=1}^{n} (PTK_i)$$

where PTK_i represents individual PTK pressure measurements and n is the number of total-pressure probes; therefore,

$$\overline{PAV} = 1/m \sum_{j=1}^{m} (PAV_j)$$

where m is the number of data samples.

Then, the maximum value minus the minimum value in this period divided by the average AIP total pressure is defined as the planar wave peak-to-peak value. It can be expressed in equation form as follows:

$$PW(pk\text{-}pk) = [\max(PAV) - \min(PAV)] / \overline{PAV}$$

Turbulence

The inlet turbulence parameter is the average of the root-mean-square of the total pressure fluctuations at each PTK divided by the AIP time-averaged total pressure.

$$TU - 1/n \sum_{i=1}^{n} \left\{ 1/m \sum_{j=1}^{m} [(PTK_j - \overline{PAV})/(\overline{PAV})]^2 \right\}^{1/2}$$

where n is the number of total pressure measurements included in the average, and m denotes the number of data samples.

Recovery

Inlet recovery is described as the average total pressure at the AIP normalized to the free-stream total pressure. For the HARV Inlet Program, the inlet recovery value (REC) adds the bias-corrections described in the “In-Flight Calibration” section, and is time averaged for a given data segment.

$$REC = 1/m \sum_{i=1}^{m} (PAV/PT0)_i$$

where m denotes the number of data samples, and PT0 is the free-stream total pressure, psia.

Inlet Lip Pressure Coefficients

Pressure coefficients of the static pressure measurements about the inlet lip are calculated by taking the difference of a measured PSE static pressure and free-stream static pressure and dividing the result by the free-stream dynamic pressure. All pressure coefficients presented are time averaged for each data segment.

$$C_p = 1/m \sum_{i=1}^{m} \left(\frac{PSE - PS0}{QBAR}\right)_i$$

where m is the number of data scans, PS0 is free-stream static pressure, and QBAR is the free-stream dynamic pressure.

To determine whether a local static pressure measures supersonic conditions, the pressure coefficient corresponding to local speed of sound, C_p*, is calculated and is time averaged for each data segment.

$$C_p* = 1/m \sum_{i=1}^{m} \left\{ \left(\frac{2}{\gamma M_{\infty_i}^2}\right) \left\{ \left(\frac{(\gamma - 1)M_{\infty_i}^2 + 2}{(\gamma + 1)}\right)^{3.5} \right\} - 1 \right\}$$

REFERENCES

[1]Regenie, Victoria, Donald Gatlin, Robert Kempel, and Neil Matheny, *The F-18 High Alpha Research Vehicle: A High-Angle-of-Attack Testbed Aircraft*, NASA TM-104253, Sept. 1992.

[2]Yuhas, Andrew J., Ronald J. Ray, Richard R. Burley, William G. Steenken, Leon Lechtenberg, and Don Thornton, *Design and Development of an F/A-18 Inlet Distortion Rake: A Cost and Time Saving Solution*, NASA TM-4722, Oct. 1995.

[3]Yuhas, Andrew J., William G. Steenken, and John G. Williams, "F/A-18A Inlet Flow Characteristics During Maneuvers with Rapidly Changing Angle of Attack," presented at *5th High-Angle-of Attack Technology Conference*, Langley Research Center, Hampton, Virginia, Sept. 17–19, 1996.

[4]Steenken, William G., John G. Williams, and Andrew J. Yuhas, "An Inlet Distortion Assessment During Aircraft Departures at High Angle of Attack for an F/A-18A Aircraft," presented at *5th High-Angle-of-Attack Technology Conference*, Langley Research Center, Hampton, Virginia, Sept. 17–19, 1996.

[5]Williams, John G., William G. Steenken, and Andrew J. Yuhas, *Estimating Engine Airflow in Gas-Turbine Powered Aircraft with Clean and Distorted Flows*, NASA CR-198052, Sept. 1996.

[6]Norby, William P. and Andrew J. Yuhas, *Dynamic Distortion Prediction Using a Combined CFD/Distortion Synthesis Approach*, NASA CR-198053, Sept. 1996.

[7]"Gas Turbine Engine Inlet Flow Distortion Guidelines," *Society of Automotive Engineers Aerospace Recommended Practice*, ARP 1420, Mar. 1978.

[8]"Inlet Total-Pressure-Distortion Considerations for Gas-Turbine Engines," S*ociety of Automotive Engineers Aerospace Information Report*, AIR 1419, May 1983.

[9]*GE Distortion Analysis Program User's Manual, Version III*, General Electric Aircraft Engines, Evendale, Ohio, TM88-352, Sept. 1988.

[10]*Model Specification for F404-GE-400 Turbofan Engine*, Specification No. CP45K0006, General Electric Aircraft Engines, Evendale, Ohio, Nov. 1975, Reprinted Feb. 1983.

[11]Amin, N.F., C.J. Richards, E.G. de la Vega, and M.A. Dhanidina, *F/A-18A Engine Inlet Survey Report*, vol. I of III, Northrop Corporation, Aircraft Division, Hawthorne, California, NOR 81-316, Nov. 1981.

[12]Morse, D.B., N.F. Amin, F.W. Marxen, J.A. McGuire, E.G. de la Vega, and M. Yamada, *Propulsion System Functional and Performance Analysis Report*, Northrop Corporation, Aircraft Division, Hawthorne, California, NOR 77-364, July 1978.

[13]Moes, Timothy R. and Stephen A. Whitmore, *A Preliminary Look at Techniques Used to Obtain Airdata From Flight at High Angles of Attack*, NASA TM-101729, Dec. 1990.

[14]Ray, R.J., J.W. Hicks, and R.I. Alexander, *Development of a Real-Time Aeroperformance Analysis Technique for the X-29A Advanced Technology Demonstrator*, NASA TM-100432, May 1988.

[15]Thornton, D.A. and William G. Steenken, *Summary of Inlet Distortion Rake Activities: Flight Clearance Through High-Temperature Rake Delivery*, General Electric Aircraft Engines, Cincinnati, Ohio, NAS 3-25951, Oct. 1995.

EC91 495-15

Figure 1. NASA F/A-18A HARV aircraft (preproduction aircraft number 6) with multiaxis thrust-vectoring paddles.

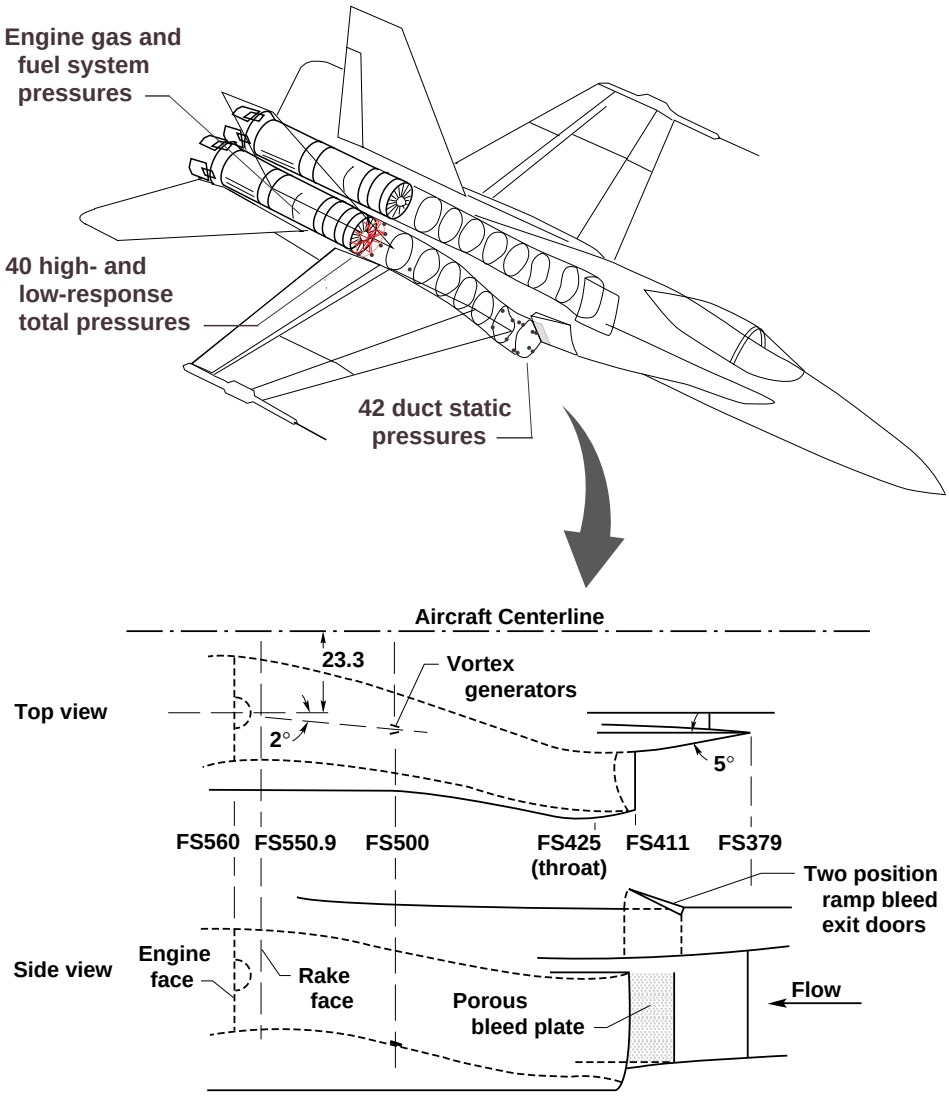

Figure 2. F/A-18A air induction system.

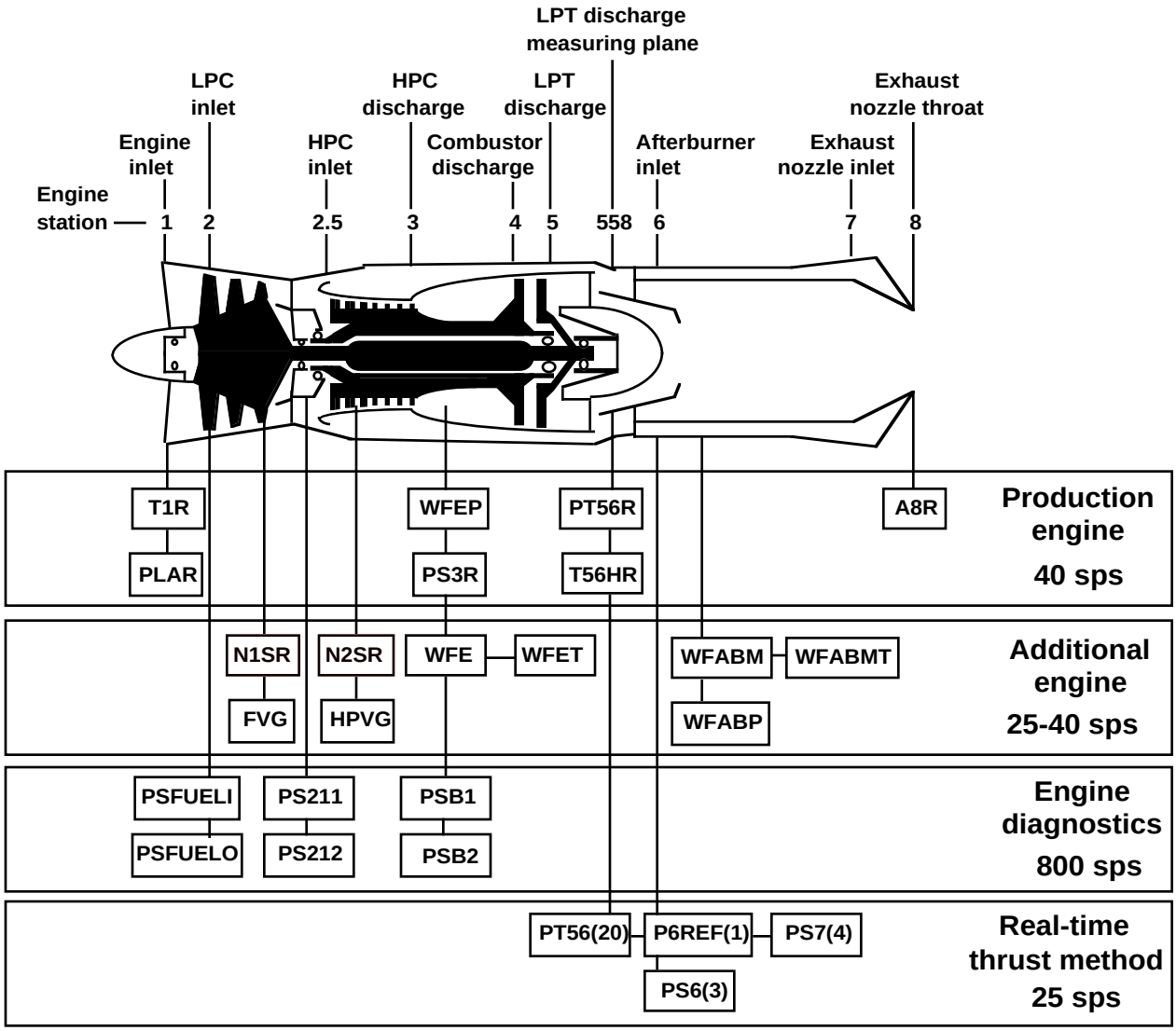

Figure 3. Right engine instrumentation used for obtaining HARV inlet research data.

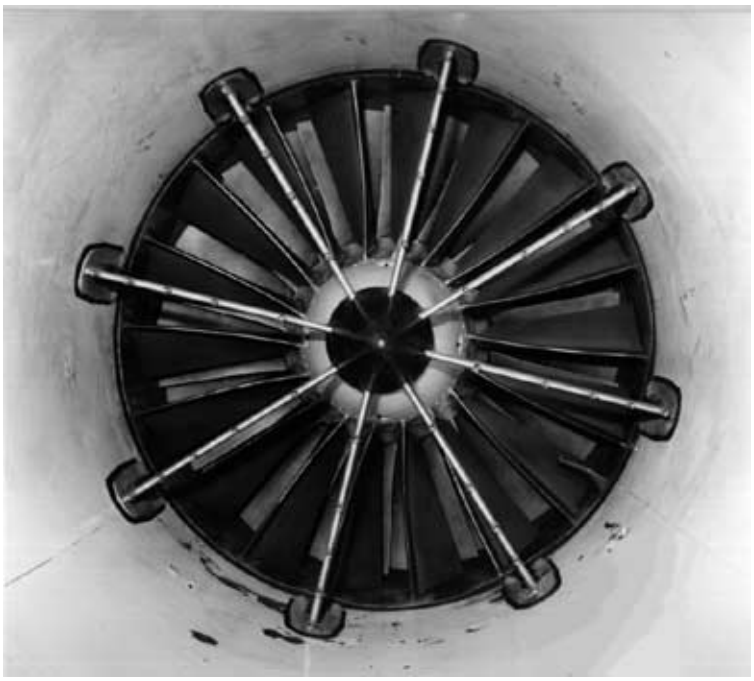

EC94 42514-11

Figure 4. NASA and GEAE inlet pressure rake mounted in the HARV right inlet with engine installed (forward-looking-aft orientation).

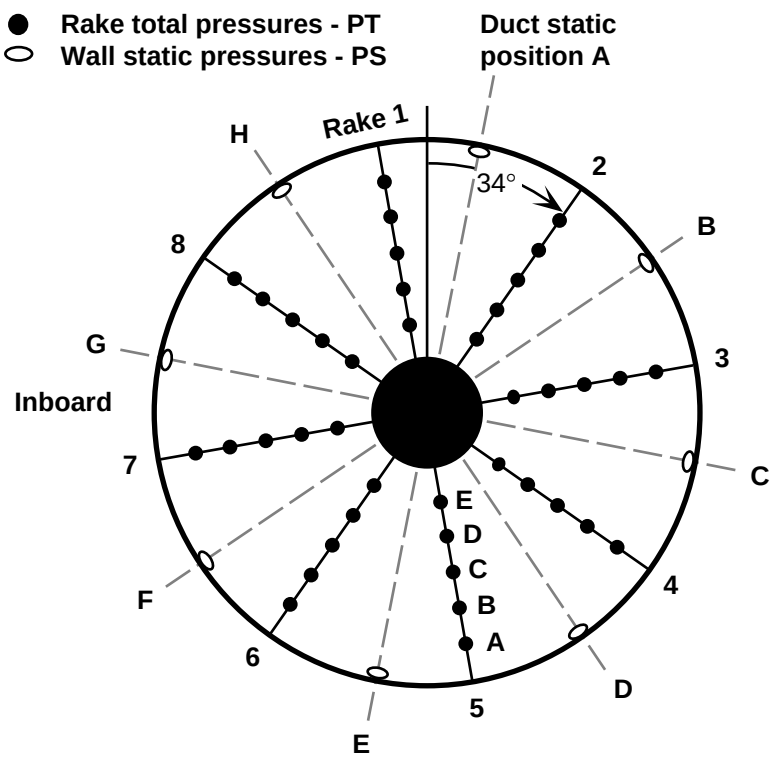

Figure 5. HARV inlet rake and duct instrumentation locations (ALF orientation).

Transducer locations

- ○ **Low response**
- ● **High response**

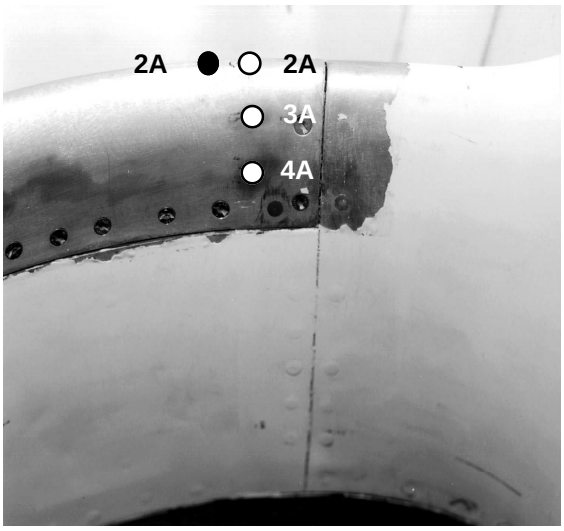

EC93 42237-8

(a) Section A, 0°, top of inlet duct entrance.

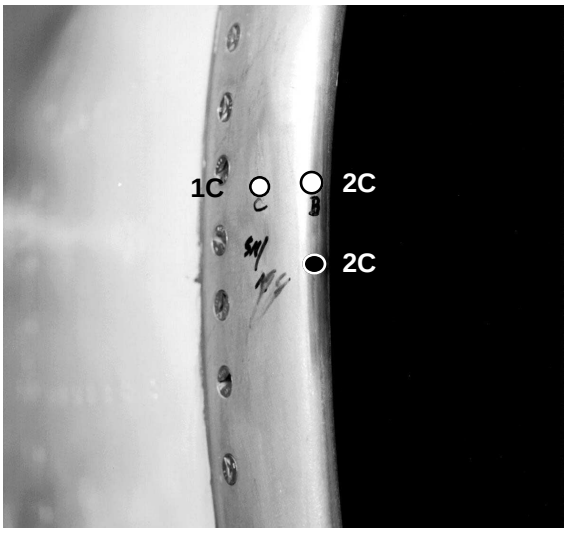

EC93 42237-5

(b) Section C, 90°, outboard side of inlet duct entrance.

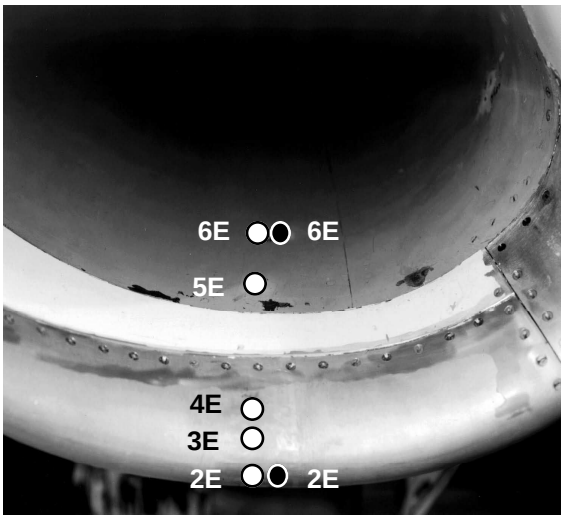

EC93 42237-4

(c) Section E, 180°, bottom of inlet duct entrance.

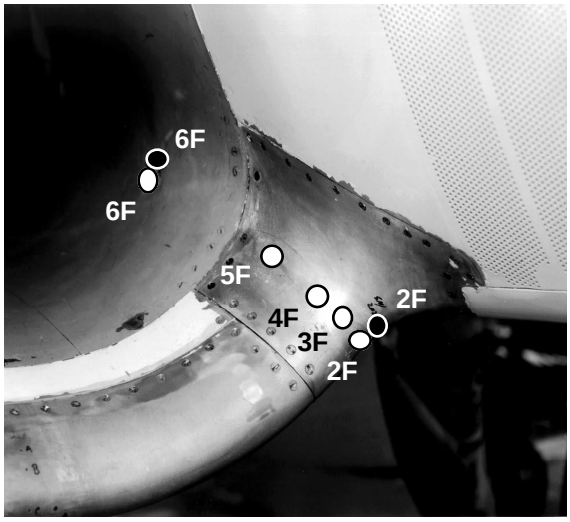

EC93 42237-3

(d) Section F, 225°, inlet and ramp junction of inlet duct entrance.

Figure 6. Inlet lip transducer locations.

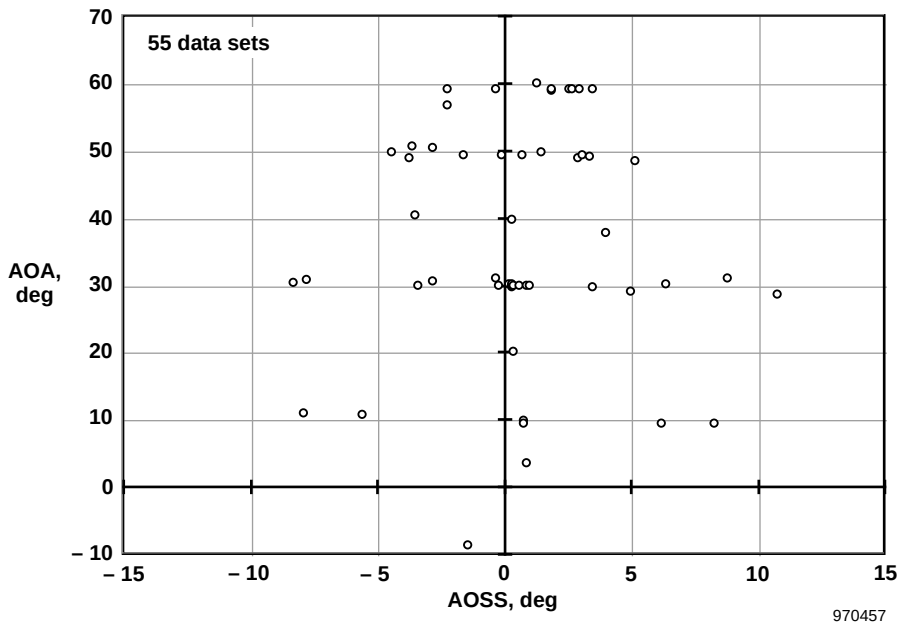

(a) Mach 0.3.

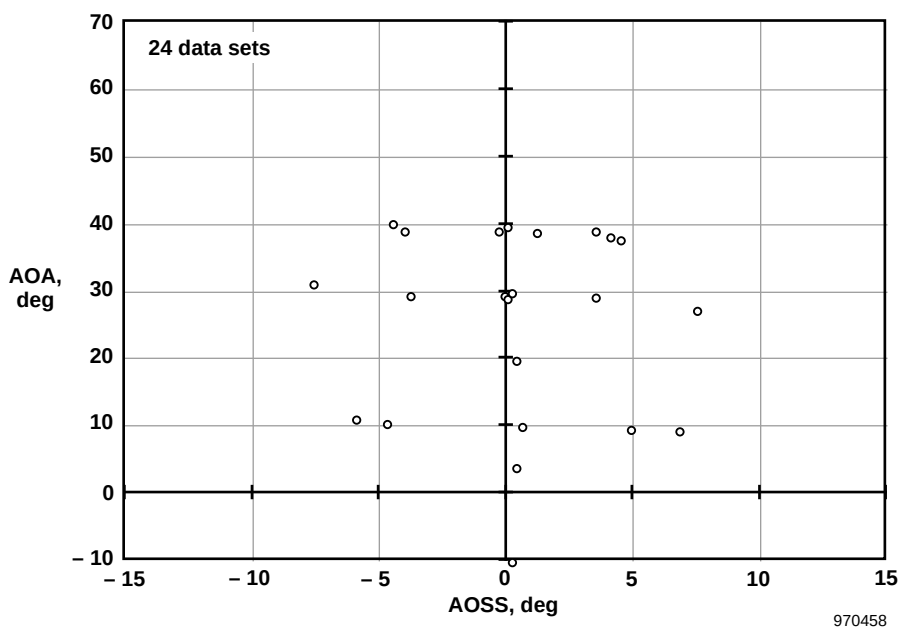

(b) Mach 0.4.

Figure 7. Inlet data obtained during fixed-attitude maneuvers, altitude ranged from approximately 20,000 to 35,000 ft, corrected engine airflow was held constant at 144 lb/sec.

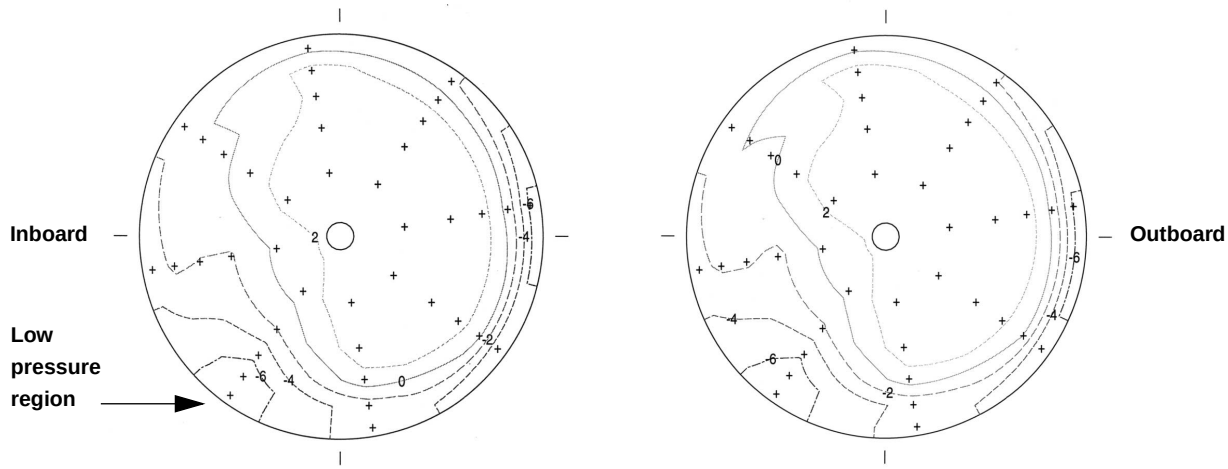

AOA = 30.0°
AOSS = 0.125°
MACH = 0.299
HPL = 25405 ft
REC = 0.971
TU = 0.007
DP/PC = 0.061
DP/PR = 0.037

(a) Flight 211.

AOA = 30.1°
AOSS = 0.002°
MACH = 0.297
HPL = 25916 ft
REC = 0.969
TU = 0.007
DP/PC = 0.062
DP/PR = 0.037

(b) Flight 213.

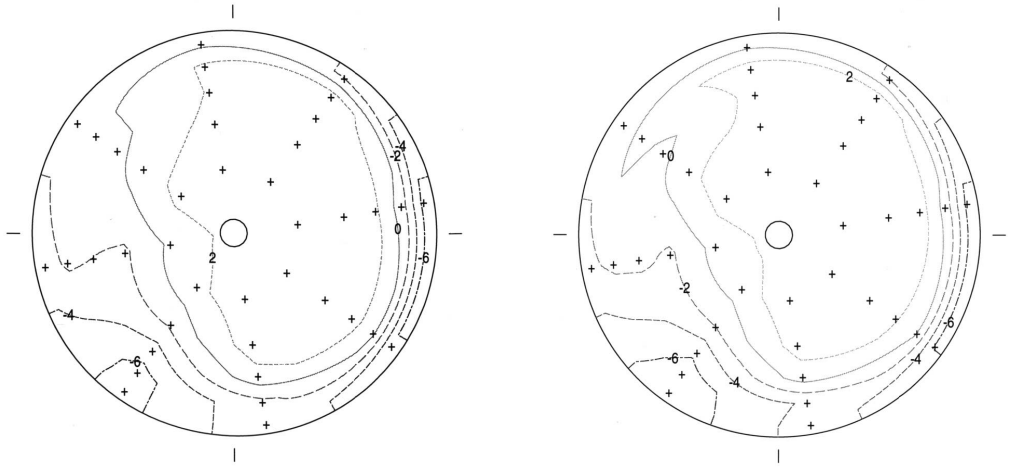

AOA = 29.6°
AOSS = 0.158°
MACH = 0.293
HPL = 21584 ft
REC = 0.972
TU = 0.007
DP/PC = 0.058
DP/PR = 0.036

(c) Flight 234.

AOA = 30.1°
AOSS = 0.171°
MACH = 0.298
HPL = 25118 ft
REC = 0.970
TU = 0.007
DP/PC = 0.060
DP/PR = 0.037

(d) Flight 241.

Figure 8. Contours of time-averaged high response total pressures showing data repeatability at Mach 0.3, AOA 30°, and AOSS 0°. ALF orientation.

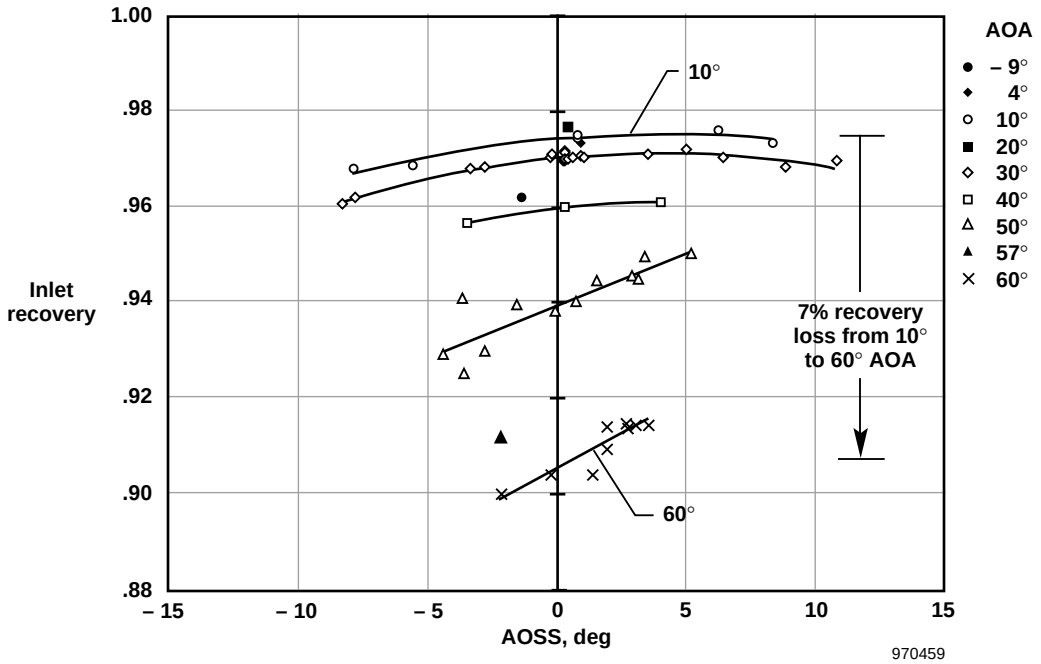

(a) Inlet recovery at Mach 0.3.

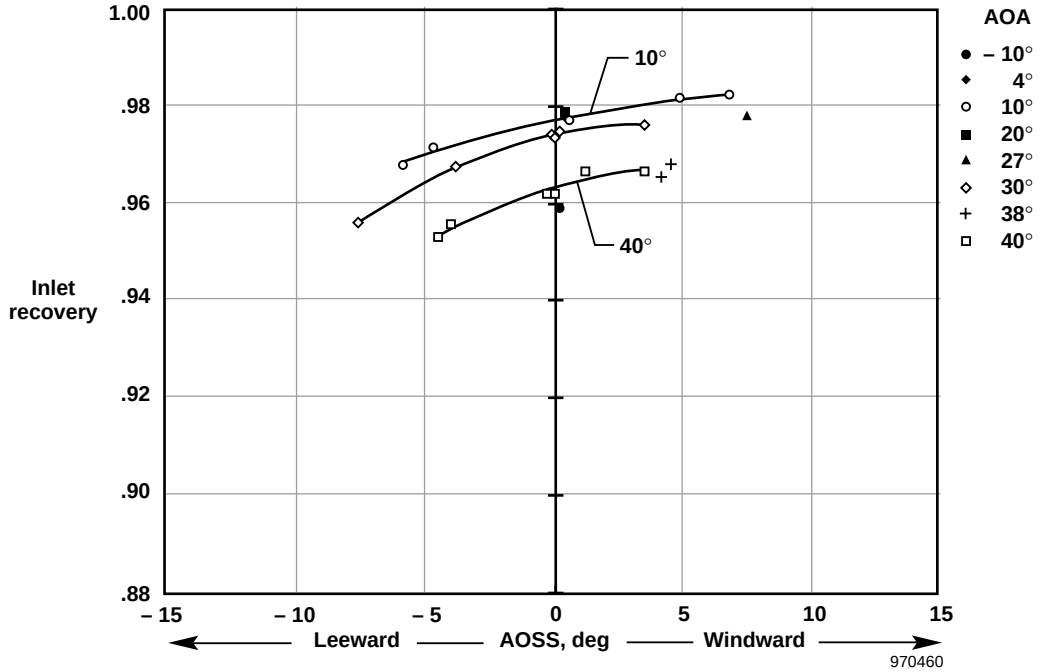

(b) Inlet recovery at Mach 0.4.

Figure 9. Effect of AOA and AOSS on inlet recovery during steady aerodynamic conditions.

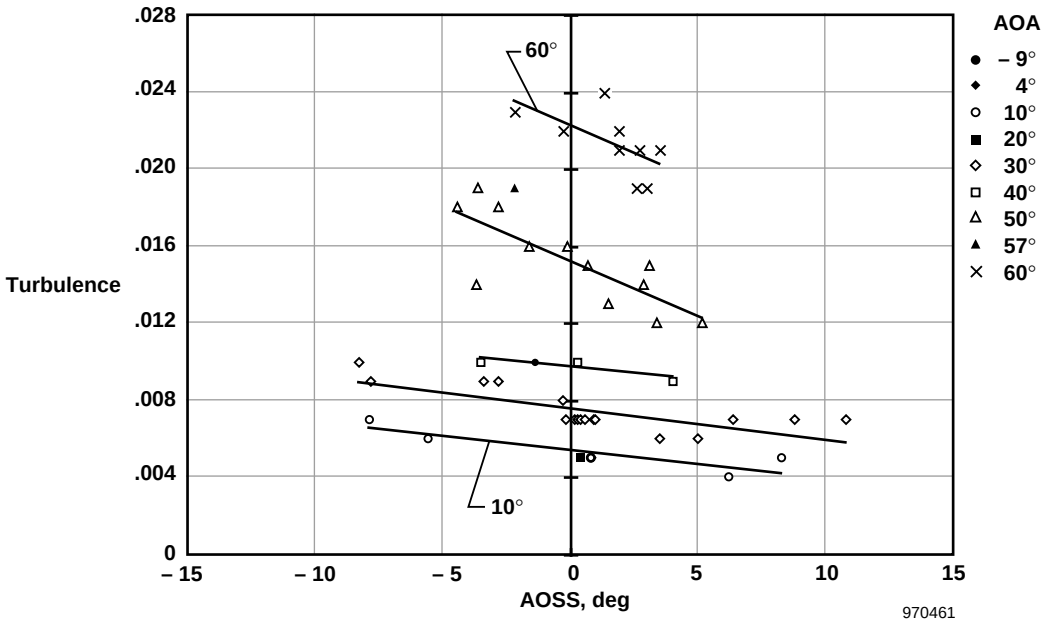

(a) Turbulence levels at Mach 0.3.

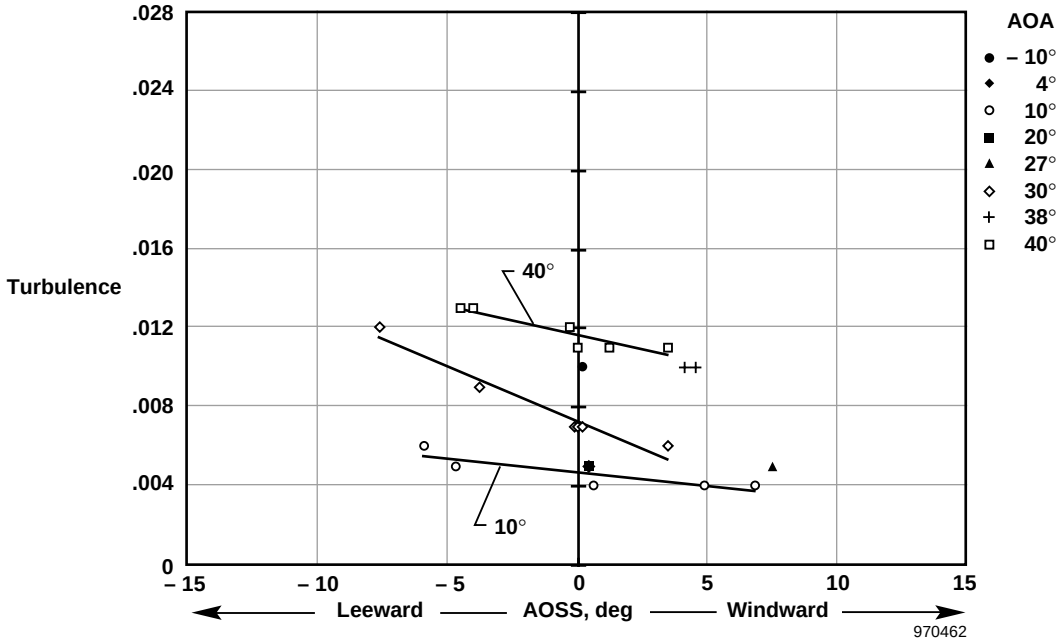

(b) Turbulence levels at Mach 0.4.

Figure 10. Effect of AOA and AOSS on turbulence levels during steady aerodynamic conditions.

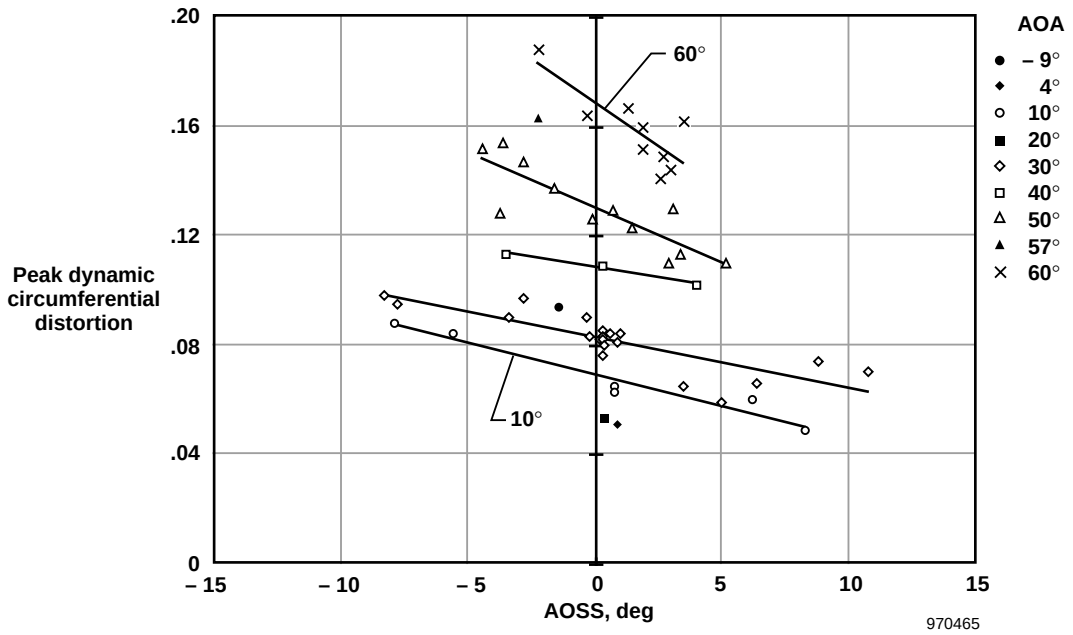

(a) Maximum dynamic circumferential distortion at Mach 0.3.

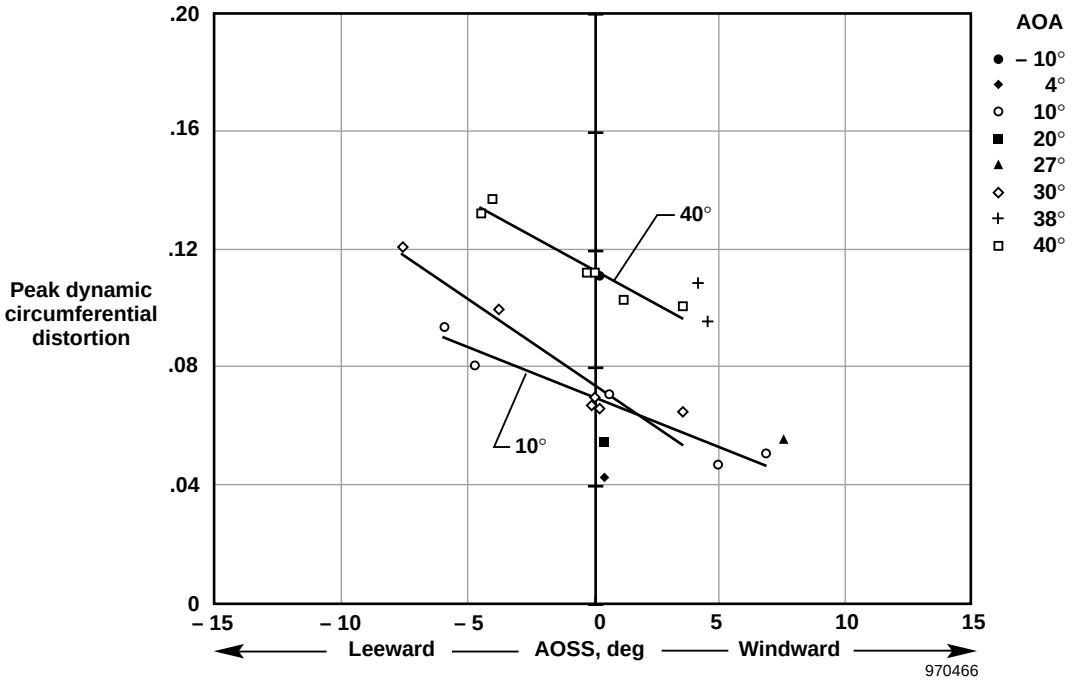

(b) Maximum dynamic circumferential distortion at Mach 0.4.

Figure 11. Effect of AOA and AOSS on maximum peak dynamic circumferential distortion during steady aerodynamic conditions.

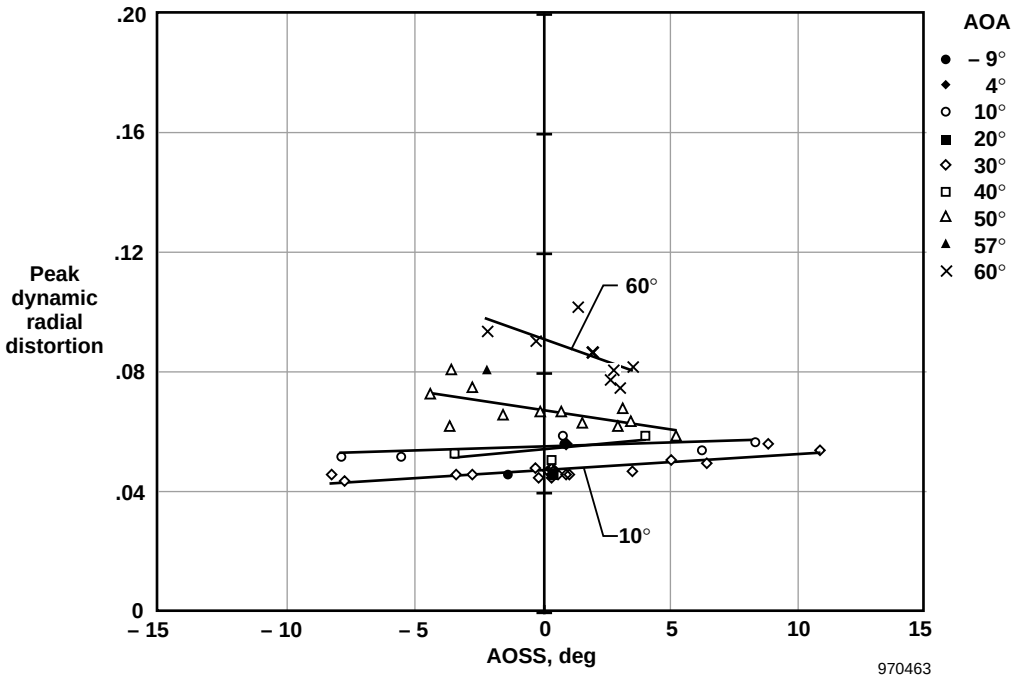

(a) Maximum dynamic radial distortion at Mach 0.3.

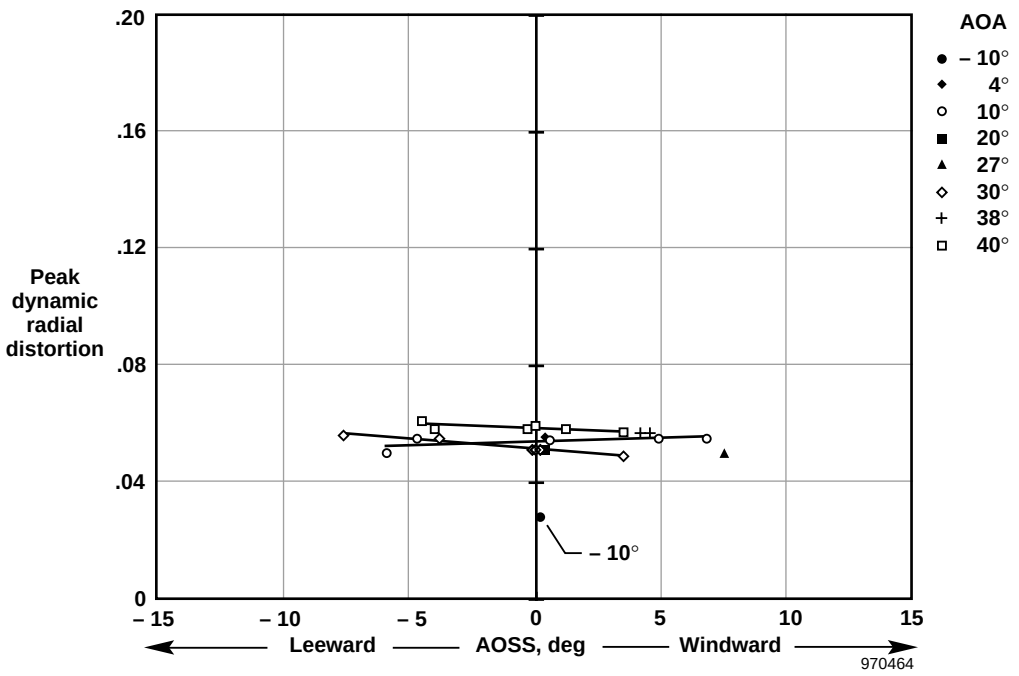

(b) Maximum dynamic radial distortion at Mach 0.4.

Figure 12. Effect of AOA and AOSS on maximum peak dynamic radial distortion during steady aerodynamic conditions.

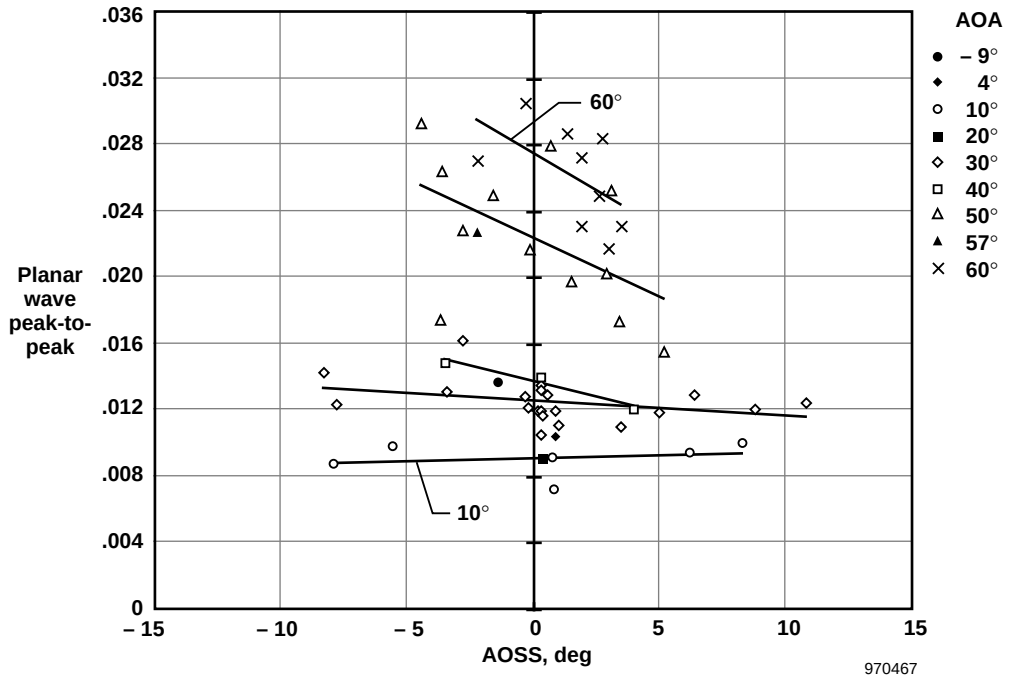

(a) Planar wave peak-to-peak fluctuations at Mach 0.3.

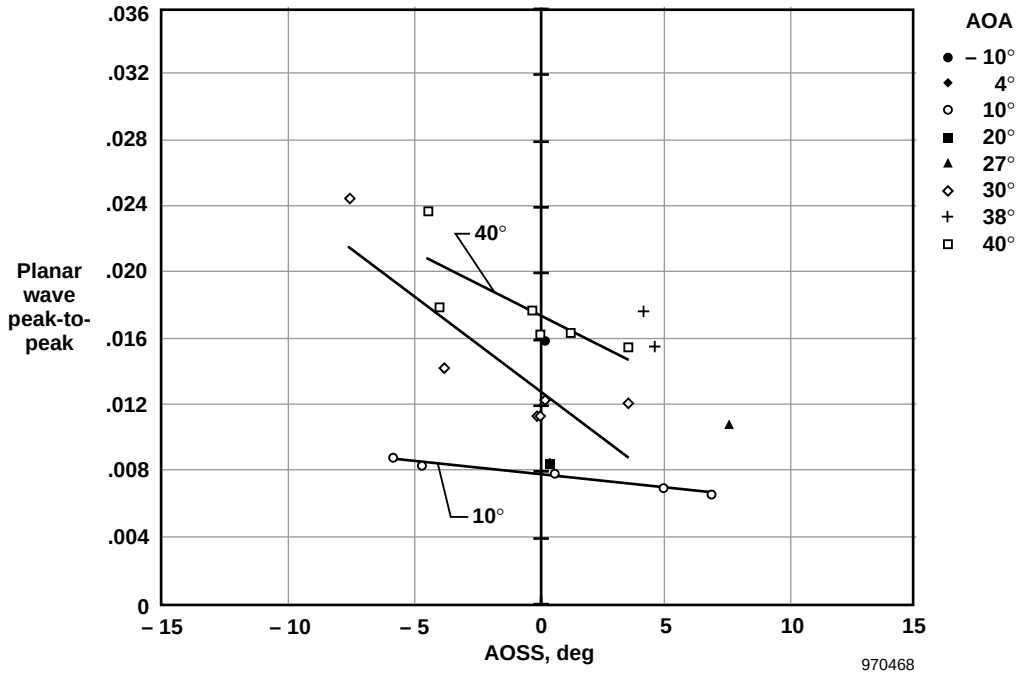

(b) Planar wave peak-to-peak fluctuations at Mach 0.4.

Figure 13. Effect of AOA and AOSS on planar wave fluctuations during steady aerodynamic conditions.

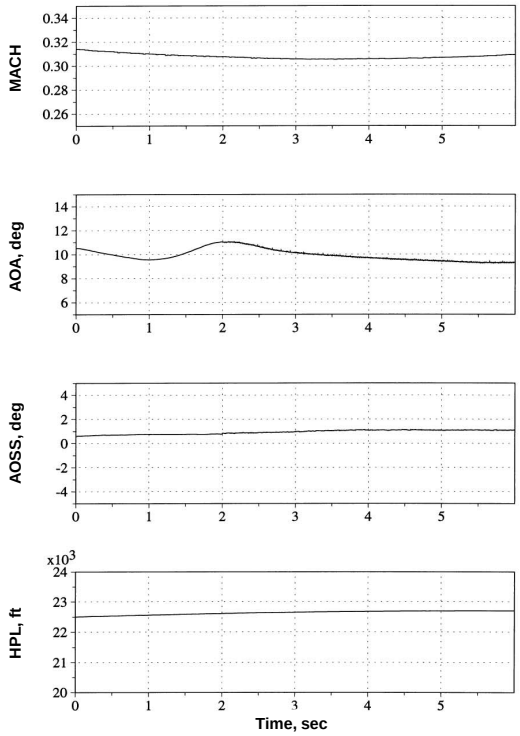

(a) Time histories of aerodynamic conditions.

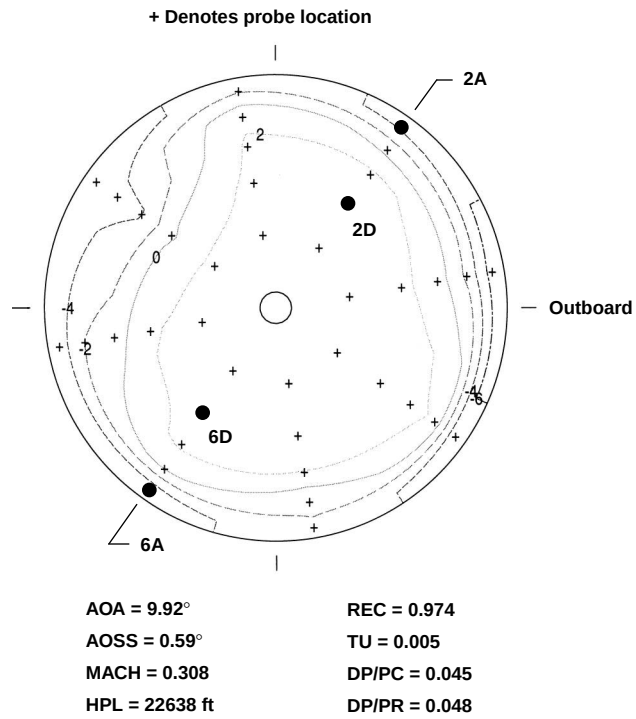

(b) Isocontours of time-averaged PTE total pressures normalized to the face average pressure.

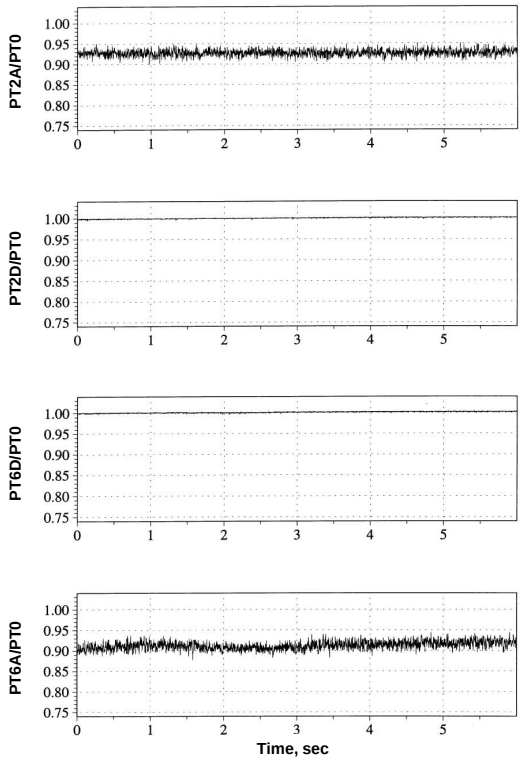

(c) Time histories of PTK inlet recoveries for rake locations 2A, 2D, 6D, and 6A.

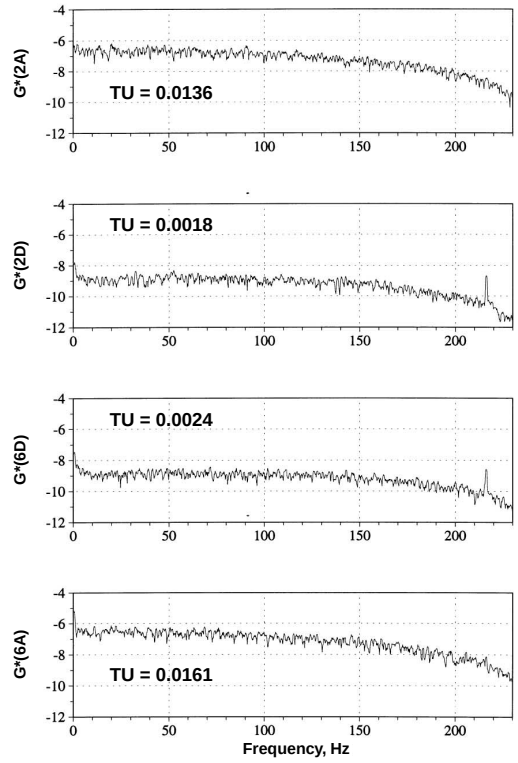

(d) PTK PSD's for rake locations 2A, 2D, 6D, and 6A.

Figure 14. AIP total pressure characteristics at AOA 10°, AOSS 0°, and Mach 0.3.

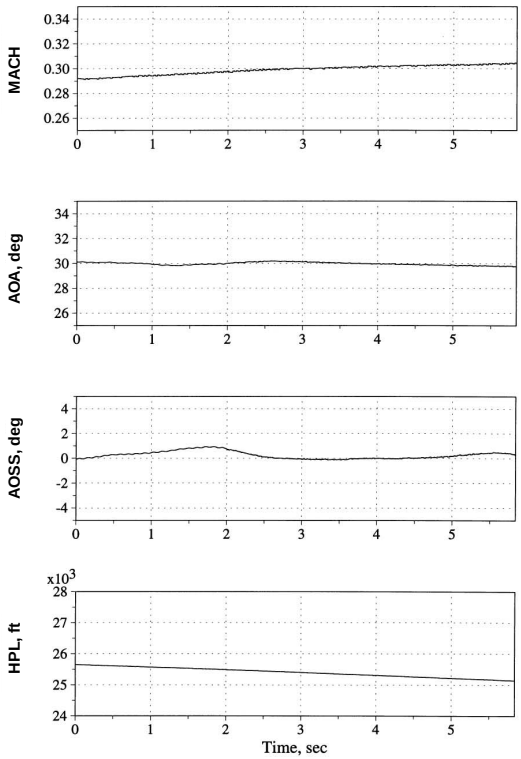

(a) Time histories of aerodynamic conditions.

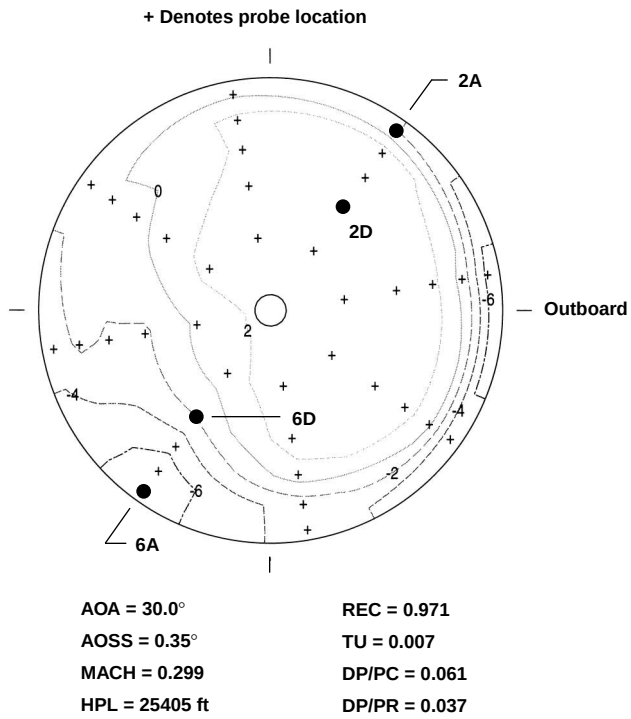

(b) Isocontours of time-averaged PTE total pressures normalized to the face average pressure.

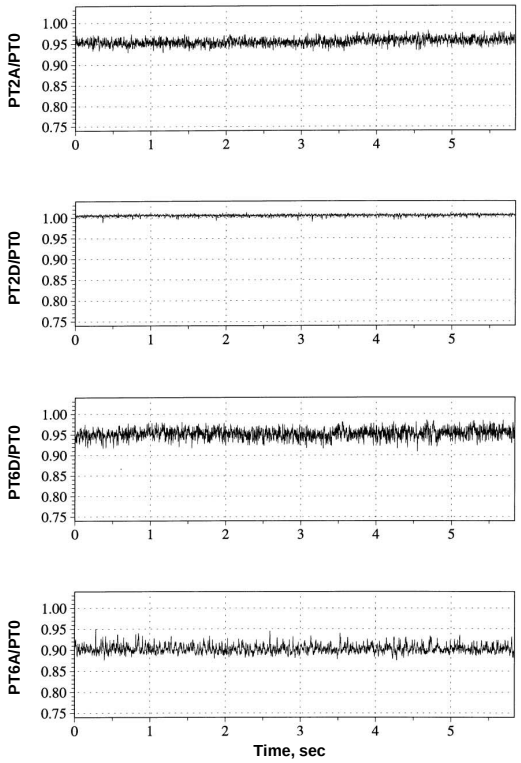

(c) Time histories of PTK inlet recoveries for rake locations 2A, 2D, 6D, and 6A.

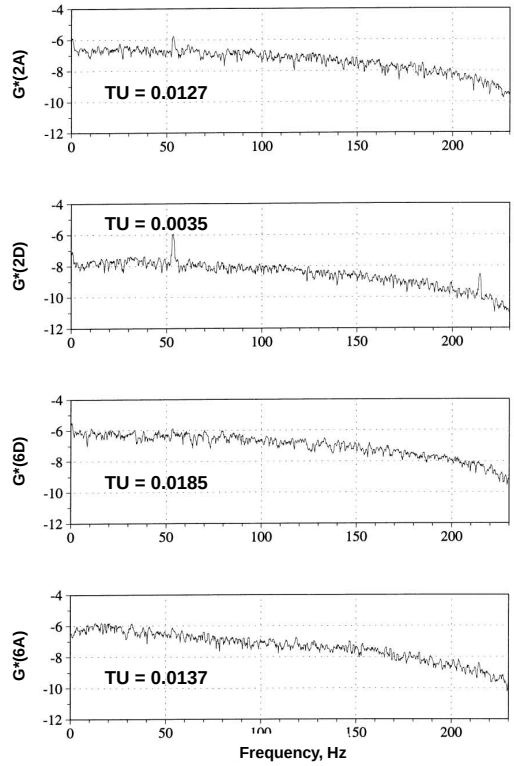

(d) PTK PSD's for rake locations 2A, 2D, 6D, and 6A.

Figure 15. AIP total pressure characteristics at AOA 30°, AOSS 0°, and Mach 0.3.

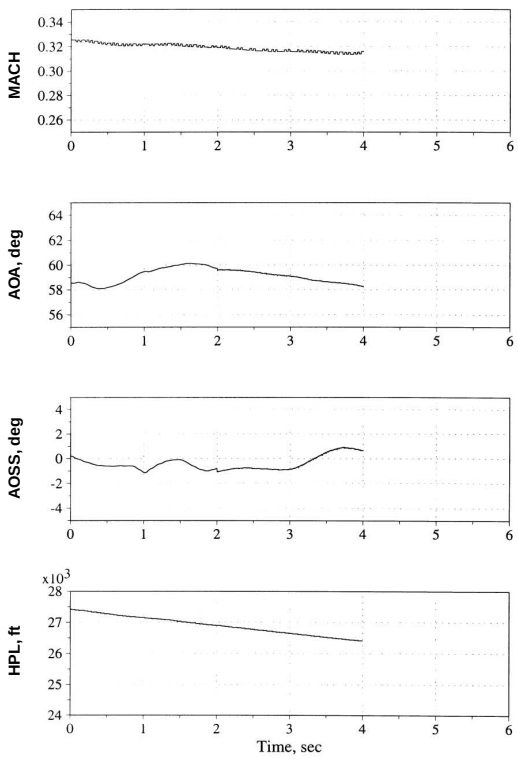

(a) Time histories of aerodynamic conditions.

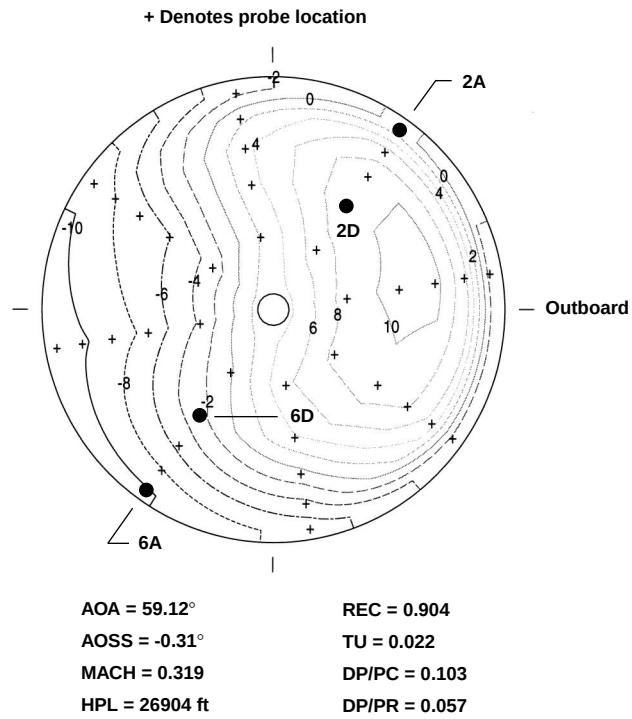

(b) Isocontours of time-averaged PTE total pressures normalized to the face average pressure

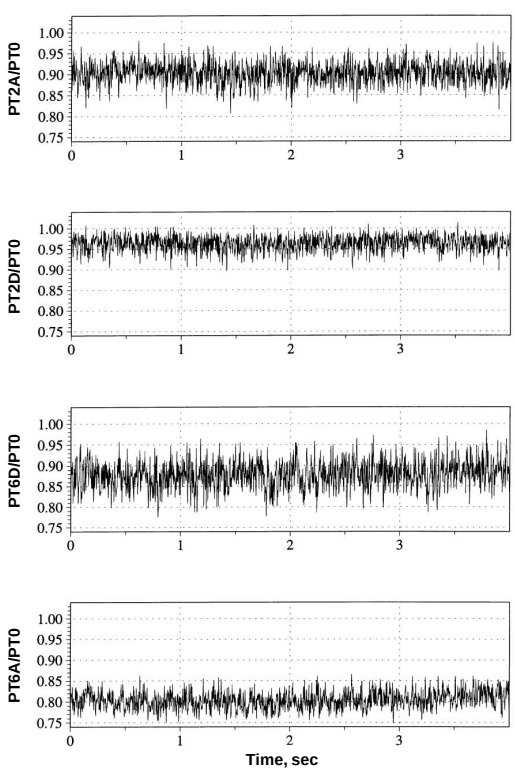

(c) Time histories of PTK inlet recoveries for rake locations 2A, 2D, 6D, and 6A.

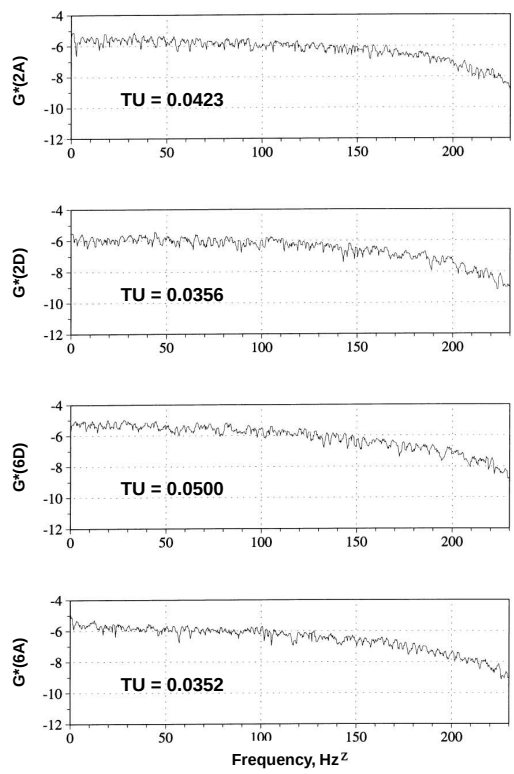

(d) PTK PSD's for rake locations 2A, 2D, 6D, and 6A.

Figure 16. AIP total pressure characteristics at AOA 60°, AOSS 0°, and Mach 0.3.

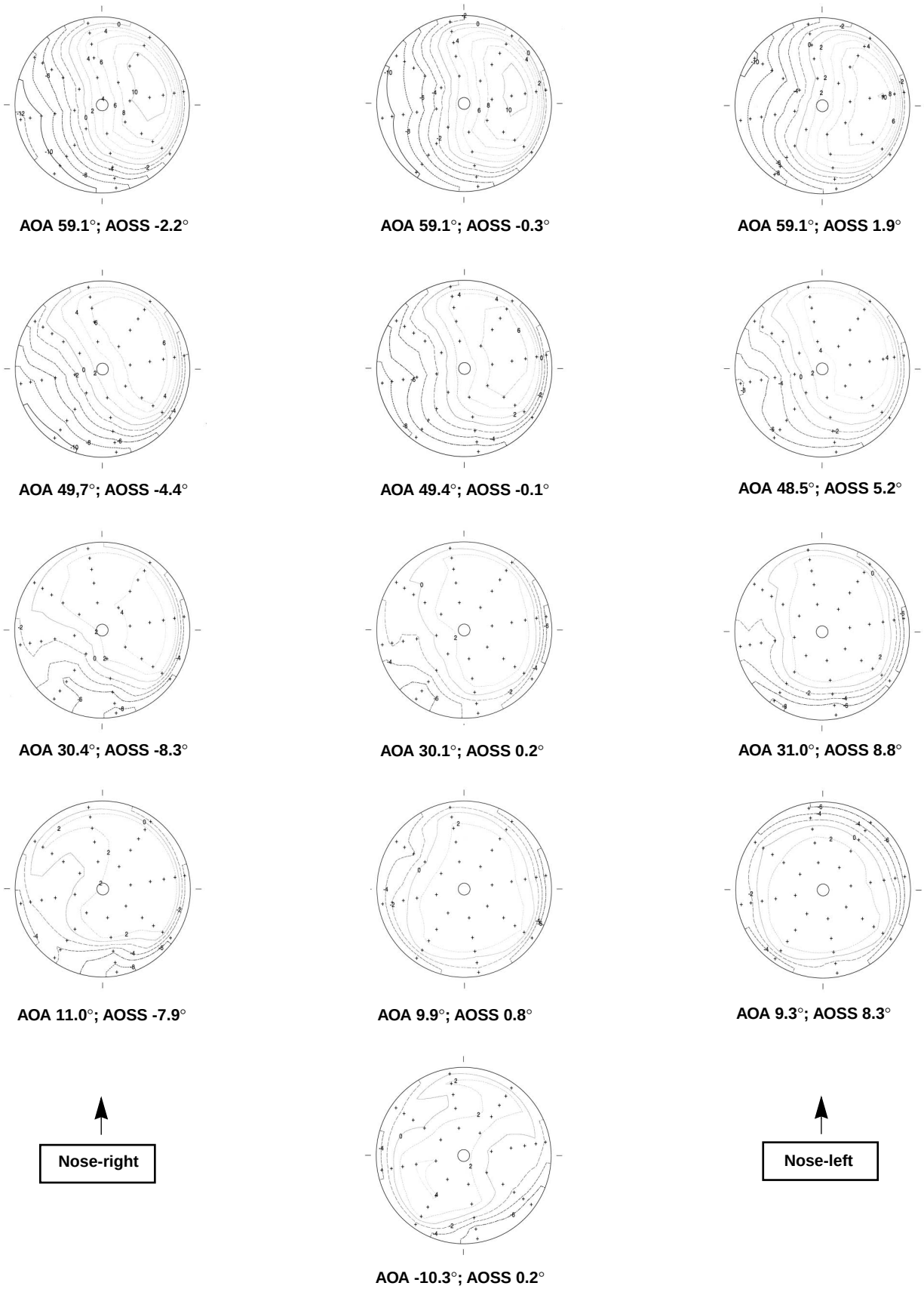

Figure 17. Contours of AIP total pressures for a range of AOA and AOSS.

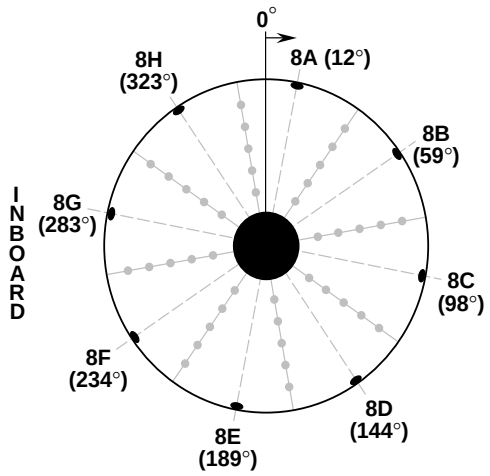

(a) AIP wall-static pressure locations.

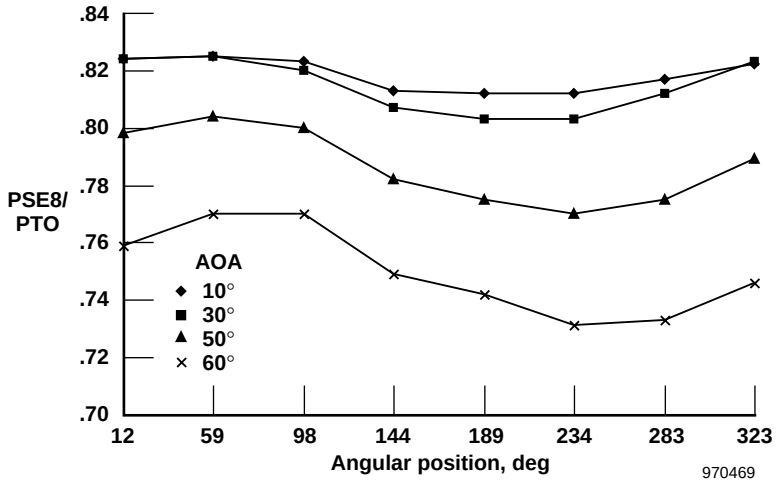

(b) Effect of AOA on ESP wall pressures at the AIP, AOSS 0°.

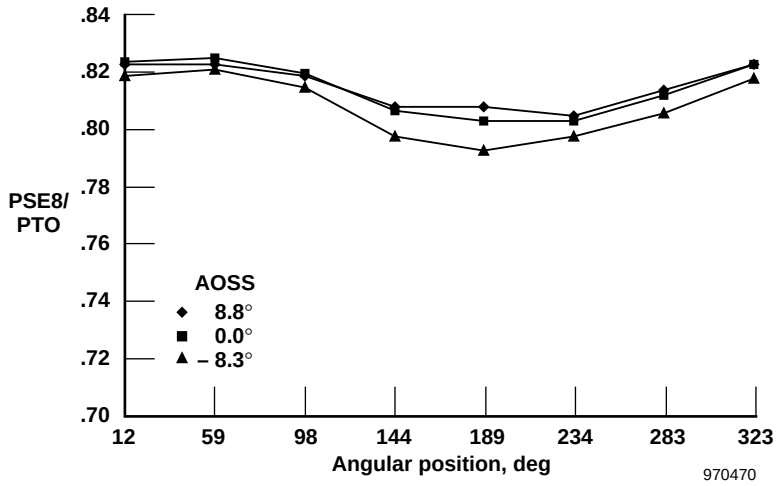

(c) Effect of AOSS on ESP wall pressures at the AIP, AOA 30°.

Figure 18. Effect of AOA and AOSS on averaged wall static pressures at the AIP, Mach 0.3.

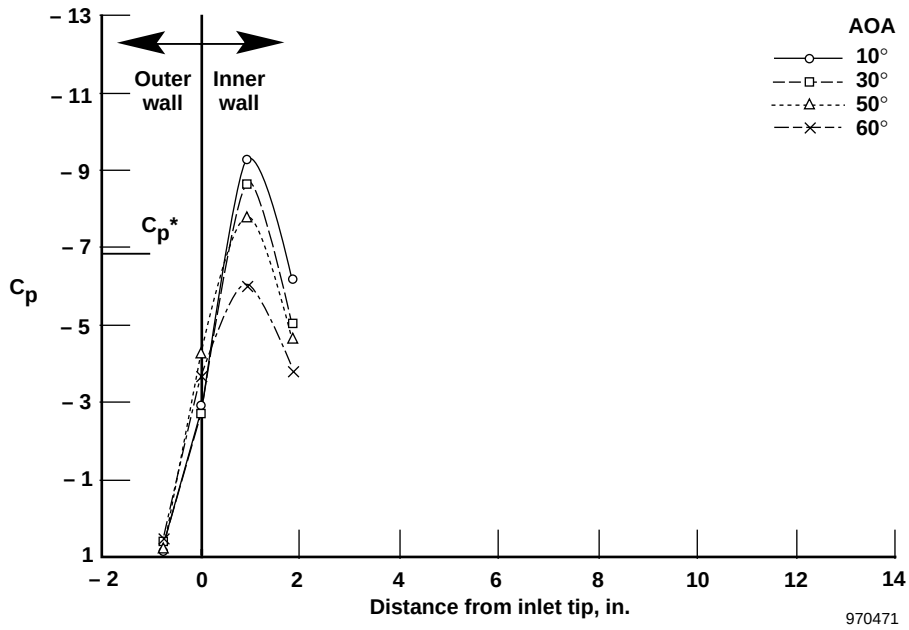

(a) A-rows: 0 degrees; top of duct.

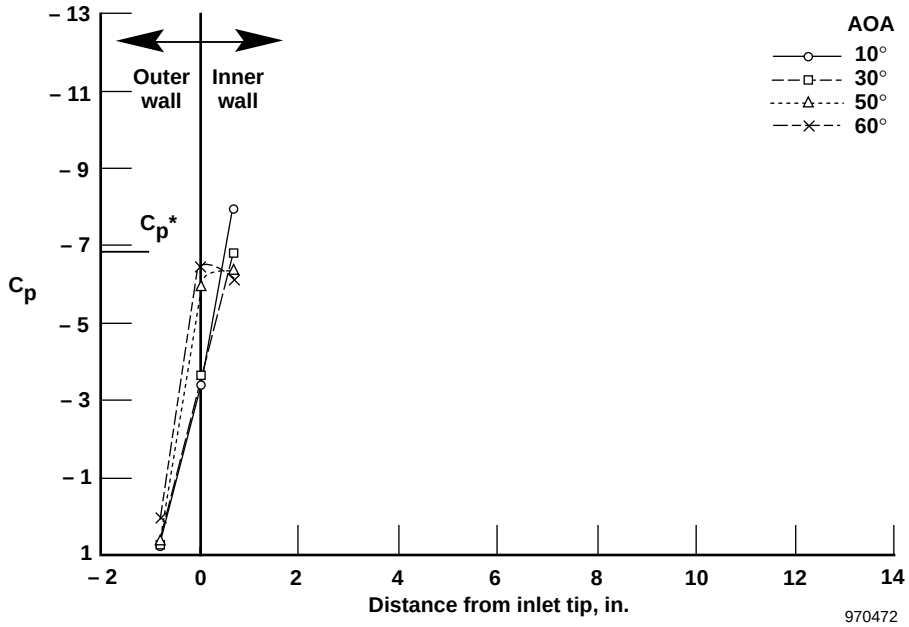

(b) C-rows: 90 degrees; side of duct.

Figure 19. Comparison of inlet lip surface pressures at AOA 10°, 30°, 50°, and 60°; AOSS 0°, and Mach 0.3

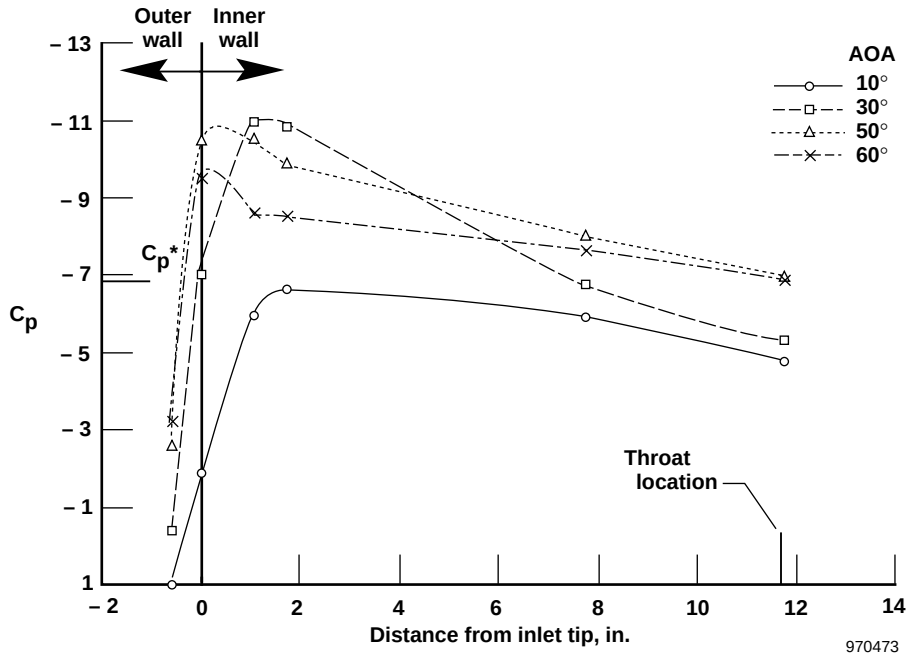

(c) E-rows: 180 degrees; bottom of duct.

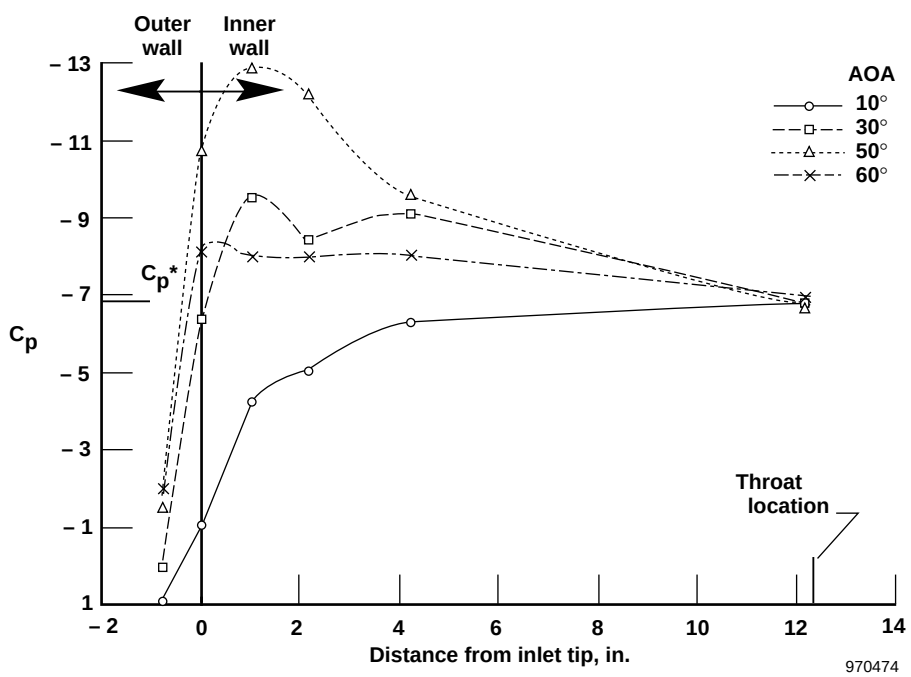

(d) F-rows: 225 degrees; wing/cowl junction.

Figure 19. Concluded

REPORT DOCUMENTATION PAGE

Form Approved
OMB No. 0704-0188

Public reporting burden for this collection of information is estimated to average 1 hour per response, including the time for reviewing instructions, searching existing data sources, gathering and maintaining the data needed, and completing and reviewing the collection of information. Send comments regarding this burden estimate or any other aspect of this collection of information, including suggestions for reducing this burden, to Washington Headquarters Services, Directorate for Information Operations and Reports, 1215 Jefferson Davis Highway, Suite 1204, Arlington, VA 22202-4302, and to the Office of Management and Budget, Paperwork Reduction Project (0704-0188), Washington, DC 20503.

1. AGENCY USE ONLY (Leave blank)

2. REPORT DATE
April 1997

3. REPORT TYPE AND DATES COVERED
Technical Memorandum

4. TITLE AND SUBTITLE
Inlet Distortion for an F/A-18A Aircraft During Steady Aerodynamic Conditions up to 60° Angle of Attack

5. FUNDING NUMBERS
529 31 04 00 37 00 F-18

6. AUTHOR(S)
Kevin R. Walsh, Andrew J. Yuhas, John G. Williams, and William G. Steenken

7. PERFORMING ORGANIZATION NAME(S) AND ADDRESS(ES)
Analytical Services & Materials, Inc.
Edwards, California

General Electric Aircraft Engines
Cincinnati, Ohio

8. PERFORMING ORGANIZATION REPORT NUMBER
H-2171

9. SPONSORING/MONITORING AGENCY NAME(S) AND ADDRESS(ES)
NASA Dryden Flight Research Center
P.O. Box 273
Edwards, California 93523-0273

10. SPONSORING/MONITORING AGENCY REPORT NUMBER
NASA TM-104329
NASA Contract NAS 3-26617

11. SUPPLEMENTARY NOTES
Presented at the High-Angle-of-Attack Technology Conference, NASA Langley Research Center, Hampton, Virginia, Sept. 17–19, 1996. This report is available on-line on the NASA Dryden Technical Report Server, http://www.dfrc.nasa.gov/cgi-bin/DTRS/dtrs.pl

12a. DISTRIBUTION/AVAILABILITY STATEMENT
Unclassified—Unlimited
Subject Category 07

12b. DISTRIBUTION CODE

13. ABSTRACT (Maximum 200 words)

The effects of high-angle-of-attack flight on aircraft inlet aerodynamic characteristics were investigated at NASA Dryden Flight Research Center, Edwards, California, as part of NASA's High Alpha Technology Program. The highly instrumented F/A-18A High Alpha Research Vehicle was used for this research. A newly designed inlet total-pressure rake was installed in front of the starboard F404-GE-400 engine to measure inlet recovery and distortion characteristics. One objective was to determine inlet total-pressure characteristics at steady high-angle-of-attack conditions. Other objectives include assessing whether significant differences exist in inlet distortion between rapid angle-of-attack maneuvers and corresponding steady aerodynamic conditions, assessing inlet characteristics during aircraft departures, providing data for developing and verifying computational fluid dynamic codes, and calculating engine airflow using five methods. This paper addresses the first objective by summarizing results of 79 flight maneuvers at steady aerodynamic conditions, ranging from –10° to 60° angle of attack and from –8° to 11° angle of sideslip at Mach 0.3 and 0.4. These data and the associated database have been rigorously validated to establish a foundation for understanding inlet characteristics at high angle of attack.

14. SUBJECT TERMS
FA-18A aircraft, High angle of attack, Inlet distortion, Pressure distributions, Steady aerodynamic conditions

15. NUMBER OF PAGES
50

16. PRICE CODE
AO3

17. SECURITY CLASSIFICATION OF REPORT
Unclassified

18. SECURITY CLASSIFICATION OF THIS PAGE
Unclassified

19. SECURITY CLASSIFICATION OF ABSTRACT
Unclassified

20. LIMITATION OF ABSTRACT
Unlimited